이학석사 학위논문

Structural Transitions in Alumina and Aluminate Glasses and Melts: Implication for Crystallization of Magma Ocean

고상 핵자기 공명 분광분석을 이용한
비정질 알루미나 결정화 과정의 반응속도론 연구:
마그마 바다의 결정화 과정에 관한 원자 단위의 고찰

2013 년 2 월

서울대학교 대학원
지구환경과학부
류 새 봄

Structural Transitions in Alumina and Aluminate Glasses and Melts: Implication for Crystallization of Magma Ocean

고상 핵자기 공명 분광분석을 이용한
비정질 알루미나 결정화 과정의 반응속도론 연구:
마그마 바다의 결정화 과정에 관한 원자 단위의 고찰

지도 교수 이 성 근

이 논문을 이학석사 학위논문으로 제출함
2012 년 12 월

서울대학교 대학원
지구환경과학부
류 새 봄

류새봄의 이학석사 학위논문을 인준함
2012 년 12 월

위 원 장 조 문 섭 (인)
부위원장 허 영 숙 (인)
위 원 이 성 근 (인)

Abstract

Structural Transitions in Alumina and Aluminate Glasses and Melts: Implication for Crystallization of Magma Ocean

Saebom Ryu

School of Earth and Environmental Sciences

The Graduate School

Seoul National University

Understanding the structure and disorder of prototypical oxide glasses provides improved insights into geochemical processes involving magmas in the Earth's surfaces and interiors. Al_2O_3, one of the archetypical covalent oxides, is not a glass-former, unlike most other covalent oxides such as SiO_2, GeO_2, and B_2O_3, hence an amorphous phase cannot be obtained by conventional melt-quenching. Amorphous Al_2O_3 can be formed as thin films through varying deposition processes, such as physical vapor deposition (PVD) and atomic layer deposition. It can also be synthesized through hydrolysis of Al-organic ligands by sol-gel process.

Whereas full understanding of atomic arrangements of amorphous Al_2O_3 has remained an unsolved problem due to the lack of suitable experimental probes of amorphous oxide surfaces, progress in high-resolution 2-dimenional solid-state NMR techniques (*e.g.* 3QMAS) enables us to explore previously unknown details of Al coordination environments in oxide glasses. Lee *et al.* (2009) reported the first Al-27 3QMAS NMR spectra for physically and chemically deposited Al_2O_3 glass and the species distribution is remarkably similar to what has been predicted theoretically for Al_2O_3 melts (Lee *et al.*, 2009; Lee *et al.*, 2010).

In contrast to a small sample volume typically ~nm-μm-thick films of amorphous Al_2O_3 through thin film deposition, sol-gel synthesis of Al_2O_3 glass using aluminum lactate as an attractive precursor yields much larger sample volume, shedding light on a new opportunity to collect an NMR spectrum with significantly improved signal/noise ratio. This allows us to explore the detailed temperature-induced structural transitions in amorphous alumina. Hydrolysis of Al-lactate at room temperature was accompanied by the annealing of the transparent xerogel at approximately 720 K. ^{27}Al 3QMAS NMR spectrum for the sol-gel synthesized Al_2O_3 glass exhibits well resolved Al coordination environments, characterized with mostly $^{[4,5]}$Al and a minor fraction of $^{[6]}$Al. This species distribution shows the remarkable similarity to that of thin films, suggesting narrow stability of amorphous states in the amorphous Al_2O_3.

The unique temperature-induced structural changes in amorphous Al_2O_3 have been observed. The fraction of $^{[5]}$Al decreases with increasing annealing time and temperature. We show, for the first time, that two distinct processes (structural transitions within glass and crystallization) can indeed be

experimentally observed by probing the fraction of $^{[5]}$Al. The results also demonstrate that structural transition relevant to the annihilation of $^{[5]}$Al within amorphous network is kinetically favored compared with structural rearrangement during crystallization of amorphous oxides. We also found that the estimated activation energy for each process may depend on the presence of potential residual carbon phases (*e.g.*, residual organic ligand) and presence of hydration shell as has been suggested from the previous studies on crystallization kinetics. Despite the uncertainty in the estimated activation energy barrier, ln $\boldsymbol{k}$ decreases linearly with increasing 1/T suggesting that each process can be described with Arrhenius behaviors.

The current results highlight the first detailed estimation of crystallization kinetics of the archetypal Al_2O_3 on the basis of its atomic scale structural evolution. Additionally, the experimental results, for the first time, revealed the presence of two distinct mechanisms for structural rearrangement upon crystallization in the prototypical single-component oxide glasses. The current results and method can shed light on a new opportunity to study crystallization kinetics of diverse natural and multi-component silicate glasses and melts. The potential result may yield atomic-level understanding of Earth's chemical evolution.

Keywords: amorphous Al_2O_3, solid-state NMR, crystallization kinetics, magma ocean

Student Number: 2009-22950

Table of Contents

List of Figures

Figure 9| ^{27}Al 3QMAS NMR spectra for Al_2O_3 annealed for 2 h at 873 K, 923 K, 973 K, 1038 K and 1073 K. Contour lines are drawn at 5% intervals from relative intensities of 8% to 98% with an added line at 4%.

Figure 10| Total isotropic projections of ^{27}Al 3QMAS NMR spectra for Al_2O_3 annealed at 973 K with varying annealing time.

Figure 11| Results of simulating Gaussian functions (black lines) of isotropic projections of the ^{27}Al 3QMAS NMR spectra for Al_2O_3 annealed at 973 K with varying annealing time. The gray lines refer to the experimental spectra rotated 30^0 clockwise.

Figure 12| Total isotropic projections of ^{27}Al 3QMAS NMR spectra for Al_2O_3 annealed at 1073 K with varying annealing time.

Figure 13| Results of simulating Gaussian functions (black lines) of isotropic projections of the ^{27}Al 3QMAS NMR spectra for Al_2O_3 annealed at 1073 K with varying annealing time. The gray lines refer to the experimental spectra rotated 30^0 clockwise.

Figure 14| Population of $^{[5]}Al$ in Al_2O_3 with annealing time.

Figure 15| X-ray diffraction (XRD) patterns of amorphous Al_2O_3 and Al_2O_3 annealed for 1, 3, 5, 10, 20 and 120 min at 1073 K.

Figure 16| X-ray diffraction (XRD) patterns of Al_2O_3 annealed for 2 h at 873 K, 973 K, 1038 K and 1073 K.

Figure 17| TEM images of amorphous and crystallized Al_2O_3.

Figure 18| Fractions of $^{[5]}Al$ in Al_2O_3 with annealing time at 1073 K. Red and blue lines refer to simulated mole fractions of $^{[5]}Al$ using an exponential function and Eq. 4, respectively (see text for details).

Figure 19| Fractions of $^{[5]}Al$ in Al_2O_3 with annealing time at 973 K. Red and blue lines refer to simulated mole fractions of $^{[5]}Al$ using an exponential function and Eq. 4, respectively (see text for details).

Figure 20| Arrhenius plot for Al_2O_3 annealed at 973 K and 1073 K.

Figure 21| Population of $^{[5]}Al$ in Al_2O_3 with annealing temperature.

Figure 22| ^{27}Al 3QMAS NMR spectra for Al_2O_3 annealed at 998 K (the second attempt) with varying annealing time. Contour lines are drawn at 5% intervals from relative intensities of 8% to 98% with an added line at 4%.

Figure 23| ^{27}Al 3QMAS NMR spectra for Al_2O_3 annealed at 1023 K (the second attempt) with varying annealing time. Contour lines are drawn at 5% intervals from relative intensities of 8% to 98% with an added line at 4%.

Figure 24| ^{27}Al 3QMAS NMR spectra for Al_2O_3 annealed at 1073 K (the second attempt) with varying annealing time. Contour lines are drawn at 5% intervals from relative intensities of 8% to 98% with an added line at 4%.

Figure 25| Total isotropic projections of ^{27}Al 3QMAS NMR spectra for Al_2O_3 annealed at 998 K (the second attempt) with varying annealing time.

Figure 26| Results of simulating Gaussian functions (black lines) of isotropic projections of the ^{27}Al 3QMAS NMR spectra for Al_2O_3 annealed at 998 K (the second attempt) with varying annealing time. The gray lines refer to the experimental spectra rotated 30^0 clockwise.

Figure 27| Total isotropic projections of ^{27}Al 3QMAS NMR spectra for Al_2O_3 annealed at 1023 K (the second attempt) with varying annealing time.

Figure 28| Results of simulating Gaussian functions (black lines) of isotropic projections of the ^{27}Al 3QMAS NMR spectra for Al_2O_3 annealed at 1023 K (the second attempt) with varying annealing time. The gray lines refer to the experimental spectra rotated 30^0 clockwise.

Figure 29| Total isotropic projections of ^{27}Al 3QMAS NMR spectra for Al_2O_3 annealed at 1073 K (the second attempt) with varying annealing time.

Figure 30| Results of simulating Gaussian functions (black lines) of isotropic projections of the ^{27}Al 3QMAS NMR spectra for Al_2O_3 annealed at 1073 K (the second attempt) with varying annealing time. The gray lines refer to the experimental spectra rotated 30^0 clockwise.

Figure 31| Fractions of $^{[5]}Al$ in Al_2O_3 with annealing time at 998 K (the second attempt). The relationship is simulated by using exponential functions (red and blue lines).

Figure 32| Fractions of $^{[5]}Al$ in Al_2O_3 with annealing time at 1023 K. The relationship is simulated by using exponential functions (red and blue lines).

Figure 33| Fractions of $^{[5]}Al$ in Al_2O_3 (2nd attempt) with annealing time at 1073 K. The relationship is simulated by using exponential functions (red and blue lines).

Figure 34| Population changes of $^{[5]}Al$ in Al_2O_3 annealed at 998K, 1023 K and 1073 K (the second attempt).

Figure 35| Arrhenius plot for Al_2O_3 annealed at 998 K, 1023 K and 1073 K (the second attempt).

Figure 36| ^{17}O MAS NMR spectra for sol-gel synthesized Al_2O_3 (black) and γ-Al_2O_3 (blue) and Na-aluminosilicate glass (red).

Figure 37| ^{17}O 3QMAS NMR spectra for sol-gel synthesized Al_2O_3 (left) and γ-Al_2O_3 (right).

Figure 38| Atomistic model for amorphous Al_2O_3 cluster including $^{[3]}O$. Gray, red, white atoms are Al, O, H, respectively. (A) Starting model for amorphous Al_2O_3 cluster with 2 of $^{[5]}Al$ and 1 of $^{[4]}Al$ for the central network. (B) Result of optimization by Gaussian 03.

Figure 39| Atomistic model for $^{[3]}O$ in amorphous Al_2O_3 cluster including $^{[3]}O$. Gray, red, white atoms are Al, O, H, respectively. (A) Starting model for amorphous Al_2O_3 cluster with 3 of $^{[5]}Al$ for the central network. (B) Result of optimization by Gaussian 03.

Figure A1| ^{27}Al 3QMAS NMR spectra of pyrope ($Mg_3Al_2Si_3O_{12}$) glass. Contour lines are drawn at 5% intervals from relative intensities of 3% to 93%, with an added line at 5%.

Figure A2| ^{17}O 3QMAS NMR spectra for pyrope ($Mg_3Al_2Si_3O_{12}$) glass. Contour lines are drawn at 5% intervals from relative intensities of 3% to 93%, with an added line at 4%.

1. Introduction

1.1. Introduction

Knowledge of the atomistic structural change in amorphous oxides during their phase transition is essential for understanding evolution of the Earth from Hadean Magma Ocean (Lee *et al.,* 2008; Murakami and Bass, 2011). Crystallization of the molten Earth was undoubtedly very complex which was determined by a variety of physical and chemical processes such as convection in liquid, solid and partially molten states, crystal settling and melt extraction (Solomatov, 2007). But it is also a fundamental step to study crystallization processes in order to understand the evolution of the Earth. The detailed study of structural transitions in key oxide melts is necessary to reveal atomistic origins of changes in their macroscopic properties.

Nevertheless, a full understanding of microscopically consistent kinetics of solidification of oxide melt at both ambient and high pressure remains as a difficult question because of lack of suitable experimental probes for atomistic environment of amorphous oxides and difficulties in sample synthesis. In particular, amorphous Al_2O_3, one of important archetypical covalent oxides in the Earth such as SiO_2, has a poor glass-forming ability; hence an amorphous phase cannot be obtained by conventional melt-quenching.

However, the structure of amorphous Al_2O_3 has been revealed with thin films formed through physical vapor deposition (PVD) and atomic layer deposition (Lee *et al.*, 2009; Lee *et al.*, 2010). And various studies on atomistic structures of amorphous alumina have been conducted. In addition, it was also recently reported that amorphous alumina can be synthesized through hydrolysis of Al-organic ligands by sol-gel process (Zhang *et al.*, 2007). This method yields much larger sample volume than thin film and it allows us to explore the detailed temperature-induced structural transitions in amorphous alumina.

The fraction of $^{[5]}$Al has been used as a proxy for the degree of disorder in amorphous Al_2O_3 (Lee *et al.*, 2009). With the proxy $^{[5]}$Al, it might be possible to observe structural transitions in glass-glass and glass-crystal. Monitoring changes in the fraction of $^{[5]}$Al with structural transitions in Al_2O_3 could be the key revealing the microscopic consistent kinetics of crystallization.

1.2. Objectives

Detailed temperature-induced changes in the structure of single-component oxide magmas are easily extended to properties of natural multi-component magmatic melts which have not been well understood. The purpose of this study is to provide the atomic scale kinetic information of phase transition by observing structural changes in crystallization processes of amorphous Al_2O_3. The relaxation process of metastable amorphous materials to stable crystal

structure is predicted as a gradual process which has an observable local atomistic structural change. After the relaxation process, the equilibrium structure which has the thermodynamically lowest energy will be obtained and the process will be analyzed with kinetic variables such as time and temperature. Quantified systematic structural strains in crystallization process, we report here, would make it possible to infer microscopic constraints on geochemical evolution of Earth system involving cooling and differentiation of Magma Ocean as well as igneous rock-forming process.

1.3. Implications

Understanding the kinetics of crystallization is useful for knowing various geological phenomena because the crystallization process is ubiquitous. First, crystallization processes are related to tectonic settings. At plate boundaries where geophysical and geochemical events occur, there are structural changes in earth materials at various conditions. The phase transition at high temperature and low pressure condition occurs at convergent boundaries where plates collide and sink into the asthenosphere. Also, amorphous magma crystallizes relatively in a short time when volcanic activities typically widespread along plate margins and at hot spots occur. Second, meteorite impacts induce high temperature and high pressure environments which allow the activation energy barrier to be overcome easily. In this case, phase transitions which happen in a very short timescale are observed. This research on stages of structural transitions would be

helpful to understand the diverse phase transition in our dynamic Earth involving various compositions, temperature, pressure and time conditions.

Many researchers have been trying to reveal unknown properties of magma ocean (Tonks and Melosh, 1993; Ohtani, 1985). Particularly, studies on the crystallization of amorphous materials are essential to understand crystallization processes of melts in the magma ocean, *i.e.* the evolution of the early Earth. When transitions from melts to crystals are not events in a second, there can be observable regions that metastable amorphous materials and stable crystalline materials exist simultaneously even though they are impossible with the thermodynamic energy concept. Detailed studies on crystallization kinetics would be needed to provide better understanding of these states. Inhomogeneous element distributions in the mantle can also be studied by calculating element partitioning coefficient during the crystallization processes.

Crystallization process is important not only in geology but also in material sciences. Crystallization kinetics has been used for a long time to produce industrial glasses by suppressing crystallization. However, it was recently known that glasses can have desirable properties such as high mechanical strength, high electric resistance and small coefficient of expansion when crystals exist with glasses in an appropriate ratio (Kingery *et al*., 2006; Richerson, 1992). Thus the glass-ceramic with a proper crystallinity has become popular materials and controlling crystallization process for quick nucleation and maintaining a steady growth rate is crucial for industries. Furthermore, industrial products such as optical rewritable data storage media (Wuttig and Yamada,

2007) using a phase transition rate and properties difference between amorphous phase and crystalline phase have been developed. Thus detailed studies on crystallization kinetics will also be of importance in material sciences.

2. Backgrounds

2.1. Crystallization kinetics

Glass and crystallization

Any compound or mixture which forms a glass during cooling from the melt at a moderate cooling rate is considered to be a 'good' glassformer, while materials which require a more rapid cooling rate in order to form a glass are considered to be 'poor' glassformers. Melts which cannot be cooled to form glasses without uses of extreme cooling rates are considered to be non-glassformers. Most of single-component covalent oxides such as SiO_2, GeO_2, and B_2O_3 are good glass formers, but prototypical Al_2O_3 alone has not been classified as a glass former. Thus, the synthesis of Al_2O_3 glass is not easy particularly in quenching Al_2O_3 melts (Rosenflanz *et al.*, 2004).

Crystallization refers to a combination of nucleation and crystal growth processes. A nucleus can be either homogeneous meaning it forms spontaneously within the melt or heterogeneous meaning it forms at a pre-existing surface such as impurity, crucible wall, and etc..

There are two barriers to the formation of a nucleus. The first is the thermodynamic barrier involving the free energy change in a system when a nucleus is formed. The second is the kinetic barrier resulting from the requirement that mass be moved or rearranged in space to allow the growth of

an ordered particle (a crystal) from a disordered liquid (Shelby, 1997). The nucleation rate, $\boldsymbol{I}$ (number of nuclei per unit volume formed per unit time), is determined by the expression (James, 1985)

$$\boldsymbol{I} = A \exp[-(\Delta G^* + \Delta G_D)/k_B T] \qquad \text{(Eq. 1)}$$

where A is a constant, ΔG^* and ΔG_D are thermodynamic and kinetic free energy barriers to nucleation, respectively. ΔG^* is the work required to form a nucleus of critical size, *i.e.,* one which will grow instead of redissolving into the melt. To compare experimental data with Eq. 1, the heat capacity of the liquid was assumed equal to the heat capacity of the solid and the Stokes-Einstein approximation (Ree and Eyring, 1958; Dingwell and Webb, 1989) was used. The homogenous crystal nucleation rate $\boldsymbol{I}$ ($mm^{-3}s^{-1}$) becomes (Hammer, 2008):

$$\boldsymbol{I} = \frac{A_c}{\eta}\, T \exp\left(\frac{-16\pi\sigma^3 {T_L}^2}{3\Delta H^2 \Delta T^2 k_B T}\right) \qquad \text{(Eq. 2)}$$

where pre-exponential term A_c is a constant($=n_v k_B/3\pi\lambda^3$), η is viscosity, T is temperature, σ is the free energy associated with the crystal-liquid interface, T_L is liquidus temperature, ΔH is enthalpy of fusion, $\Delta T = T_L - T$, k_B is the Boltzmann constant.

Crystal growth can be described based on the rate controlling process of crystallization, interface controlled growth and diffusion controlled growth. If the attachment of atoms to the growing crystal face is slow compared to the migration of compatible atoms through the surrounding medium toward the

surface, growth is said to be 'interface-controlled'. The growth rate of steady-state growth $\boldsymbol{G}$ is (Turnbull and Cohen, 1960; Kirkpatrick, 1981) :

$$\boldsymbol{G} = \mathrm{f}\, a_0\, \nu \exp\left(\frac{-\Delta G'}{RT}\right) \qquad \text{(Eq. 3)}$$

where f is the fraction of site on the crystal surface available for attachment, a_o is the thickness of a growth layer, ν is the frequency of atom attachment attempts, R is the gas constant, T is temperature, $\Delta G'$ is the activation energy for attachment. If the component mobility is very slow compared to the attachment rate, then crystal growth is 'diffusion-controlled', and the growth rate $\boldsymbol{G}$ is: $\boldsymbol{G} = k(D/t)^{1/2}$ where k is a constant, D is the diffusion coefficient for the rate-controlling species in the melt (Hammer, 2008). For further information, see Shelby (1997), Hammer (2008) and Kelton and Greer (2010).

Johnson-Mehl-Avrami equation

In the Johnson–Mehl–Avrami (JMA) transformation equation where time constant (k) is expressed by the Arrhenius equation on temperature (Johnson and Mehl, 1939; Avrami, 1941), the crystallization fraction $\boldsymbol{\chi}$ is expressed as a function of time, as follows:

$$\boldsymbol{X} = 1 - \exp(-kt^n) \qquad \text{(Eq. 4)}$$

where $k = k_0\, exp(-E_a/k_B T)$. x, t, n, k_0, k_B, T, and E_a, are respectively the crystal fraction, time, Avrami exponent, preexponetial factor, Boltzmann constant, temperature, and crystallization activation energy. Here k_0, the frequency factor,

which indicates the number of attempts made by nuclei to overcome the energy barrier during crystallization. E_a is activation energy of crystallization. Avrami exponent n can be described with time dependence of nucleation n_n ($0 \leq n_n \leq 1$) and time dependence of crystal growth n_g ($1.5 \leq n_g \leq 4$): $n = n_n + n_g$ (Scott, 1983).

The general form of JMA equation is Eq. 5. The most important assumptions of this model are that there is a uniform parent phase with no crystals where nucleation occurs randomly, and that the crystals grow as spheres. Fraction crystallized $\boldsymbol{\varphi}$ ($V_{crystal}/V_{total}$)

$$\boldsymbol{\varphi} = 1 - \exp\left[-\frac{4\pi}{3}\int_{\tau=0}^{\tau=t} I_\tau \left(\int_\tau^t Y_t dt\right)^3 d\tau\right] \qquad \text{(Eq. 5)}$$

When nucleation rate I_τ and growth rate Y_t are constant,

$$1 - \boldsymbol{\varphi} = \exp\left(-\frac{\pi}{3} I Y^3 t^4\right) \qquad \text{(Eq. 6)}$$

For further information, see Kirkpatrick (1981).

2.2. Sol-gel synthesis method

Sol-gel processing allows the formation of glasses at temperatures well below those required for melting the same glasses, which helps reduce energy costs and increase purity by reducing contact with refractories. The sol-gel process is starting from a colloidal solution (or sol) that acts as the precursor for an integrated network (or gel) of either discrete particles or network polymers.

Typical precursors are metal alkoxides and metal salts (such as chlorides, nitrates and acetates), which undergo various forms of hydrolysis and condensation reactions.

In contrast to a small sample volume typically ~nm-μm-thick films of amorphous Al_2O_3 through thin film deposition, sol-gel synthesis of Al_2O_3 glass using aluminum lactate (Zhang *et al.*, 2003; Zhang and Eckert, 2004; Zhang and Eckert, 2005) yields much larger sample volume, shedding light on a new opportunity to collect an NMR spectrum with significantly improved signal/noise ratio. This allows us to explore the detailed temperature-induced structural transitions in amorphous alumina.

2.3. Experimental probes for crystallization study

Differential scanning calorimetry (DSC) and differential thermal analysis (DTA) are thermoanalytical techniques which measure temperatures and heat flows associated with physical or chemical changes in materials such as phase transitions as a function of time and temperature. DSC measures the energy required to keep system at the same temperature in both the reference and the sample whereas DTA measures the temperature difference between the sample and the reference when they are both put under the same heat. By observing these differences, quantitative and qualitative information about endothermic or exothermic processes (such as crystallization) can be provided (e.g., Kissinger, 1957; James, 1974; Gibson and Delamore, 1987). Since DSC and DTA provide

timing and temperature information for crystallization, they are useful to study kinetics of crystallization. However, they neither can provide any information about structures of materials. To study not only changes in macroscopic properties but also microscopic structural changes, other experimental probes are needed.

X-ray diffraction (XRD) is a non-destructive technique to reveal the crystallographic structure of materials with the d-spacing information. In diffraction patterns, the peak position indicates unit cell parameters and the peak intensity suggests preferred orientation and quantity. Since it is fast and easy to use in various sample types such as powder, ribbon, liquid, and thin films, it has been used widely for phase identification. There are thousands of substances in database. Crystallinity can also be identified through peak shape, thus it can be used to study crystallization kinetics. From the x-ray diffraction pattern, we can determine the moment that examinable crystalline phase is formed (*e.g.,* Zhang and Banfield, 2002). However, its limit in size makes it difficult to identify the onset of nucleation in amorphous matrix with XRD. Small structures existing only in trace amounts often go undetected by XRD readings. In addition, it is difficult to obtain the quantitative information by XRD analysis especially when amorphous phases and crystalline phases exist together. Therefore, a more accurate tool is needed to explore crystallization processes.

Vibrational spectroscopies such as IR and Raman spectroscopy produce spectra reflected vibrational modes of samples and, therefore, molecular geometry can be known by them. IR spectra tend to emphasize vibrations

involving polar bonding such as hydroxyl group while Raman spectroscopy deals with complementary bonding. Because amorphous phase which has not uniform bond angles and bond lengths shows a broad vibrational band, crystallinity can be measured with vibrational spectroscopy. However, it has a more limit to detecting crystallinity than XRD therefore more suitable for detecting not short range information but medium to long range order. Also, the laser can heat the sample that result in crystallization of the sample. Thus, vibrational spectroscopy is not the best probe for exploring quantitative atomic scale kinetics of crystallization.

Transmission Electron Microscopy (TEM) provides detailed information about crystallization kinetics with a high spatial resolution (nuclei with a size of 5 nm can be easily detected). It allows two main mechanisms in crystallization. That is, nucleation and growth to be monitored separately. Most techniques employed to determine kinetics of crystallization can measure the overall crystallization rate, but cannot probe separate contributions of nucleation and crystal growth. Crystal structures, crystal size distributions, crystal shapes, crystal orientations and defects within the crystals grown can also be assessed using TEM. One disadvantage of TEM would be that the electron beam of the TEM affects the crystallization process. In a previous study on $Ge_2Sb_2Te_5$ the electron beam was found to strongly enhance the nucleation rate, obscuring a normal (isothermal or isochronal) analysis of the transformation kinetics (Kooi *et al.,* 2004). And detailed information about structural changes such as coordination environments cannot be observed with TEM.

X-ray absorption spectroscopy [XAS = XANES (near absorption edge structure) + EXAFS (extended fine structure)] is a powerful tool to observe short range structural and chemical information in almost any physical system (gases, liquids, solids, glasses, etc.). The main advantage that XAS has is it is element specific. Spectra are collected from specific x-ray absorption edges holding information on only those species and their surroundings. Since XAS probes only short range order, it can provide structural information on amorphous materials, liquids, and gases, as well as polymer electrolytes. Thus, it is particularly useful to study the very beginnings of precipitation or crystallization. Disadvantages of XAS lie in that low-z elements are limited due to the highly attenuating sample environment and XAS is an averaging technique. XRD is useful to distinguish various phases but XAS has insensitivity to long range order.

Solid-state Nuclear magnetic resonance (NMR) techniques have many advantages in probing the atomistic kinetics of phase transitions. First, it provides element specific information which allows observing detailed atomistic structure such as coordination environments. Since the information is also quantitative, the quantitative structural changes can be obtained. Additionally, the resolution of NMR spectra is mostly higher than other spectroscopy which yields better signals to noise ratio with small sample volumes. And smaller changes in structure can be detected. Thus, unlike DSC, XRD and TEM, detailed studies on structural transitions in amorphous phase are possible. NMR technique is good for more accurate determination of the structure.

2.4. NMR spectroscopy

The NMR spectrometer is a device to magnetize the nuclear spins with a large applied magnetic field and rotate the spin polarizations by r.f. pulses for producing transverse nuclear magnetization (Levitt, 2008). Then, it detects the small oscillating electric currents induced by the precessing transverse spin magnetization. The detected NMR signal provides element specific atomic structural information such as coordination number, bond length, bond angle, connectivity and so on.

Since there are other nuclides in molecules, interactions between the magnetic field and spin interaction of neighbor nuclide make the chemical shift which has information of atomic environments. Particularly, in a solid-state sample which has shorter relaxation time than liquid, there are various quantum mechanical perturbations such as chemical shift anisotropy, dipole-dipole coupling, J-coupling, and quadrupolar coupling. These perturbations make it difficult to analyze signals by peak broadening. One of the methods to decrease the perturbation effect and to enhance the signal is magic angle spinning (MAS) NMR. MAS NMR removes chemical shift anisotropy by fixing the spinning angle (=54.7˚) during NMR experiments. As the angle dependent first-order derivation of anisotropic parameter disappears, spectra show sharp peaks and spinning side bands.

Because of advantages of NMR techniques, NMR has been used to explore topological disorder in glasses (*e.g.,* Lee *et al.*, 2001; Lee and Stebbins, 2002). Al coordination environments and topological disorder (due to bond length-angle

distribution and distortion of glass networks around Al) in aluminosilicate glasses were also revealed by the 2D triple-quantum magic-angle spinning (3QMAS) technique (*e.g.,* Lee and Stebbins, 2000; Toplis *et al.*, 2000). 3QMAS NMR technique provides enhanced resolution by using the high spinning speed of a rotor and multiple quantum coherences which suppress the second-order quadrupolar broadening (Frydman and Harwood, 1995; Baltisberger *et al.*, 1996). The 3QMAS NMR pulse sequence consists of multiple r.f. pulses and the interval between the pulses, t_1 changes during the experiment. The data acquisition time variable, t_2 and t_1 make a 2 dimensional data matrix. t_2 leads to MAS dimension and t_1 isotropic dimension by making the Fourier transform (Levitt, 2008). This technique has been successfully used, to yield a quantitative fraction of Al coordination environments and structural sites in aluminosilicate glasses at ambient and high pressure (*e.g.,* Lee *et al.*, 2004; Lee and Stebbins, 2006). In the present study, 2D 3QMAS NMR is used to quantify the fraction of Al coordination environments.

3. The Effect of Temperature and Time on Structural Transitions in Amorphous Al_2O_3

3.1. Previous works

Structural changes in glasses

The fractional melting and crystallization are major processes to control the thermal state and evolution of the mantle which determine the distribution of geochemical species in the Earth's interior. There are many studies on changes in properties and atomistic structures during the phase transition of silicate melts and glasses (Gaudio *et al.*, 2008; Lee *et al.*, 2008). Stixrude and Karki (2005) reported the presence of neutrally or negatively buoyant melt in the deep mantle and provided a possible means to be used for large-scale chemical differentiation and a natural explanation for the ultralow velocity zone at the base of the mantle. Lee (2011) studied the densification mechanism of CNAS melts and suggested the Si-rich hidden reservoir which can be a possible missing Si content in primary mantle.

A majority of studies on nucleation were conducted in simple systems (compositionally) and reported to the materials science society for the synthesis of industrial glasses and ceramics (Hammer, 2008). In order to interpret the crystallization process of magma, materials such as Li_2O-SiO_2 and Na_2O-2CaO-$3SiO_2$ were considered as model system of silicate melts (*e.g.*, James, 1974; Kelton and Greer, 1988; Davis and Ihinger, 2002). One of the simplest geologically

relevant melts, Al_2O_3, has not been studied well because of its poor glass forming ability. In this study, for the first time, crystallization process of amorphous Al_2O_3 has been studied in atomic scale as a model system of magma ocean.

Structure of Amorphous Aluminum Oxide

Despite its importance, the structure of alumina has not been well understood because of lack of suitable experimental probes for atomistic environment of Al_2O_3 and difficulties in sample synthesis. Amorphous Al_2O_3 cannot be obtained by conventional melt-quenching because alumina is not a glass former. However, amorphous phases can be formed as thin films through vapor deposition. Lee *et al.* (2009) and Lee *et al.* (2010) revealed the structure of amorphous Al_2O_3 with chemically and physically deposited thin films with using developed 3Q MAS NMR techniques.

3.2. Experiments

3.2.1. Sample Preparation

Sol-gel method

To prepare amorphous Al_2O_3, 0.004 mol (1.18 g) solid aluminum L-lactate (97%, Sigma Aldrich) was dissolved into 40 ml distilled water. The solution became transparent after 5~10 min stirring with a stirring machine (Figure 1-A).

The pH range of the solution was 3.48 and it corresponds to the optimum pH range suggested by Zhang *et al.* (2007; pH 1.8~4.0). In this hydrolysis process, Zhang *et al.* (2007) used 10 ml distilled water to dissolve 1.18 g aluminum L-lactate but we used 40 ml water in order to remove organics easily in the next condensation stage. The clear colorless solution was spread out on the flat glass plate (Figure 1-B) and dried at room temperature over 5 days (Figure 1-C). After natural air drying, the xerogel was collected (Figure 1-D) and the powder was placed in a platinum crucible and heated from room temperature to 723 K with a furnace (Figure 1-E) to take organics and water away. In the furnace, the sample was heated for 200 min with increasing heating temperature from room temperature to 423 K (37.5 K/h) and for 6 h at constant heating temperature 423 K, and then, for 16 h with increasing heating temperature from 423 K to 723 K (18.75 K/h). At first, in order to find these heating conditions ideal for making the amorphous Al_2O_3, the powder was collected in a beaker and heated on a hot plate. The beaker was heated from 343 K to 423 K with the heating temperature rising when there was no more decrease in the weight of samples. Then it maintained over 2 days at 423 K. The color of samples changed from white to yellowish brown at 363 K, and dark brown at around 423 K. The dark brown samples turned light-colored after further heating to 723 K by 30 K per hour in the platinum crucible (Figure 1-F). These color changes are different from previous experiments (Zhang *et al.,* 2007). Darkening of samples during heating to 423 K may have been caused by unburned organics. Further changes into lighter colors seemed to indicate that the removal of organics. The ratio of water to aluminum L-lactate controlled the color of samples, but ^{27}Al MAS NMR spectra patterns of samples found to be the same regardless of dissolving ratio

and their NMR characterizations correspond to previous experimental results (Zhang *et al.*, 2007).

Annealed amorphous samples

To prepare samples undergone structural transitions, sol-gel synthesized amorphous Al_2O_3 was annealed at various temperature and time conditions. Conditions for annealing temperature and time were set at 896 K for 1, 2, 3, 5, 10 and 120 min, at 973 K for 1, 3, 5, 10, 30, 60, 90 and 120 min, and at 1073 K for 1, 3, 5, 10, 20, 30, 60 and 120 min. Samples annealed at 873 K, 923 K and 1028 K for 2 h were prepared additionally. Annealing conditions were set up based on the crystallization onset temperature suggested (Lee *et al.*, 2009). We repeated crystallization experiments in order to check the reproducibility. Annealing conditions of the second experimental set were at 998 K for 5, 15, 30, 45, 60, 120 min, 3, 6, 9, 12, 24 and 48 h, and at 1023 K for 2, 4, 6, 8, 10, 30, 60, 120 min, 3, 4, 5 and 6 h, at 1073 K for 2, 4, 6, 8, 10, 12, 15, 20, 30, 60, 90 and 120 min. Samples were placed in the platinum crucible and annealed in the furnace. Annealing time was measured from the moment the crucible put into the furnace.

3.2.2. NMR spectroscopy

^{27}Al NMR spectra were collected on a Varian 400 solid-state spectrometer (9.4 T) at a Larmor frequency of 104.23 MHz with a 3.2 mm zirconia rotor in a

Varian double-resonance probe. A relaxation delay of 0.5 s and an r.f. pulse length of 0.3 μs were used to collect the 1D ^{27}Al MAS spectrum. The 2D ^{27}Al triple quantum (3Q) MAS NMR spectra of amorphous and partially crystallized Al_2O_3 were collected using a fast-amplitude modulation (FAM)-based shifted-echo pulse sequence (0.5 s relaxation delay-3.0 μs pulse for 3Q excitation-t_1 delay-FAM pulse train with a 0.6 μs pulse-echo delay-a 15 μs soft pulse for echo reconversion-t_2 acquisition). Collection time of a sample for 1D spectrum was about 8 min and that for 2D spectra was about 4 h. About 14 mg samples were packed in the rotor and sample spinning speed was 18 kHz. NMR spectra were referenced to $AlCl_3$ solution.

3.3. Results and Discussion

3.3.1. Al-27 MAS & 3QMAS NMR Results

Figure 3 presents the ^{27}Al MAS NMR spectra of sol-gel synthesized Al_2O_3 and annealed samples at 896 K for 1, 2, 3, 5, 10 and 120 min. The features at approximately 60, 35, 0 ppm are observed. These features are due to distinct Al coordination environments such as four-, five-, and six-coordinated aluminums (*i.e.*, $^{[4]}Al$, $^{[5]}Al$, and $^{[6]}Al$) (*e.g.*, Stebbins *et al.*, 2000). The sol-gel synthesized Al_2O_3 has Al coordination environments which are mostly $^{[4,5]}Al$ and a small fraction of $^{[6]}Al$. It is the feature of amorphous Al_2O_3, which is quite similar to the coordination environments of Al_2O_3 thin films (Lee *et al.*, 2009; Lee *et al.*, 2010). The temperature-induced structural changes with heating at 896 K for 1 min to 2

h are very small but an increasing signal intensity of $^{[6]}$Al peak with increasing annealing duration is observable.

Figure 4 shows the ^{27}Al MAS NMR spectra for Al_2O_3 annealed at 973 K for 1, 3, 5, 10, 30, 60, 90 and 120 min. Significant changes in the distribution of peak intensity with increasing annealing time are observed. Unlike 896 K annealing, for 2 h annealing, changes in Al coordination environments with decreasing fraction of $^{[5]}$Al (~35 ppm) is clearly observed. After 10 min annealing at 973 K, the peak at ~ 0 ppm ($^{[6]}$Al) became larger than the peak at ~ 35 ppm ($^{[5]}$Al).

In Figure 5, we can see the ^{27}Al MAS NMR spectra for Al_2O_3 annealed at 1073 K for 1, 3, 5, 10, 20, 30, 60 and 120 min. Dramatic structural changes in amorphous Al_2O_3 are revealed. Much faster transitions than in samples annealed at 973 K are shown. After 30 min annealing at 1073 K, the $^{[5]}$Al feature is negligible very likely to be seen $^{[4]}$Al and $^{[6]}$Al. This feature is similar to that of the ^{27}Al MAS NMR spectra for γ-Al_2O_3 (Huggins and Ellis, 1992). It indicates the fraction of $^{[5]}$Al could be a proxy for crystallization in Al_2O_3.

Figure 6 shows the ^{27}Al MAS NMR spectra for Al_2O_3 annealed for the same duration time (1, 5, 10, 60 and 120 min) at different temperature (896 K, 973 K and 1073 K) which shows briefly effects of time and temperature on structural transitions of amorphous alumina. The black, red and blue lines are for the samples annealed at 896 K, 973 K, and 1073 K, respectively. There is no big difference depending on temperatures in changing atomistic environments up to 5 min annealing. After 10 min annealing, however, the features of 3 different samples annealed for the same amount of time proved to be quite distinct. The

difference in temperature effect on structural transitions in amorphous Al_2O_3 between 973 K and 1073 K seems much larger than those of between 896 K and 1073 K.

Al-27 3QMAS NMR Results

Figure 2 shows the ^{27}Al 3QMAS NMR spectra for Al_2O_3. Figure 2(A) is for sol-gel synthesized Al_2O_3 and Figure 2(B) for amorphous Al_2O_3 thin film (Lee *et al.*, 2009). ^{27}Al 3QMAS NMR spectrum for the sol-gel synthesized Al_2O_3 glass exhibits well resolved Al coordination environments, characterized by mostly $^{[4,5]}Al$ and a minor fraction of $^{[6]}Al$. The presence of a significant amount of $^{[5]}Al$ confirms the amorphous nature of sol-gel synthesized Al_2O_3. In addition, the species distribution of sol-gel synthesized Al_2O_3 shows the remarkable similarity to those of thin films suggesting narrow stability of amorphous states in the amorphous Al_2O_3.

Figure 7 and 8 show the two-dimensional ^{27}Al 3QMAS NMR spectra for Al_2O_3 annealed at 973 K and 1073 K with varying annealing time. Unlike 1D MAS NMR spectra, well resolved features in 3QMAS NMR spectra yield unambiguous coordination environments, making available the quantitative analysis for each coordination species. Before heat treatments, the fraction of $^{[5]}Al$ in sol-gel synthesized Al_2O_3 seemed to be about 50%. With 973 K annealing, it became about 20% after 20 min. But it just took 10 min to have the similar fraction with 1073 K annealing. Also, the coordination environments for γ-Al_2O_3 which has

only $^{[4]}$Al and $^{[6]}$Al are observed in samples annealed at 1073 K over 30 min. This feature may indicate the onset of crystallization.

Figure 9 shows the ^{27}Al 3QMAS NMR spectra for Al_2O_3 annealed for 2 h at different temperatures (873 K, 923 K, 973 K, 1038 K and 1073 K). Contour lines are drawn at 5% intervals from relative intensities of 8% to 98% with added line at 4%. Abrupt transition in partially crystallized samples is shown between 923 K and 973 K annealing samples. This suggests the existence of sudden decreasing $^{[5]}$Al region in annealing conditions.

Figure 10 and 12 present total isotropic projections of ^{27}Al 3QMAS NMR spectra for Al_2O_3 annealed at 973 K and 1073 K with varying annealing time. The fraction of $^{[5]}$Al decreases and $^{[4]}$Al, $^{[6]}$Al increases with annealing. The gradual changes are observed which suggests decreasing in the extent of disorder. Isotropic projections of 3QMAS NMR were used to calculate the fractions of $^{[4, 5, 6]}$Al in **3.2.3.**.

3.3.2. Data simulation and kinetic models for transitions

The NMR signal intensity in the 3QMAS NMR experiment is determined by efficiencies in triple quantum excitation and single quantum reconversion that are mostly dependent on the magnitude of the interactions between the nuclear quadrupolar moment and the electric field gradient (*i.e.*, P_q). The observed NMR signal intensity was, therefore, scaled to take into consideration the magnitude of the quadrupolar interactions characteristic of each Al coordination environment

by numerical simulations (Baltisberger *et al.*, 1996). This method has been successfully used to yield a quantitative fraction of Al coordination environments and structural sites in aluminosilicate glasses at ambient and high pressure (Lee, 2004; Lee *et al.*, 2004; Lee and Stebbins, 2009).

Figure 11 and 13 show the results of a simulation with 3 Gaussian peaks of the total isotropic projection of the ^{27}Al 3QMAS NMR spectra. Isotropic projection spectra have been adjusted with a shearing value 12 μsec (rotated about 30^0 clockwise) to make spectra more fitted in Gaussian functions. Peaks in Figure 11 and 13 (gray lines) are symmetric as compared with Figure 10 and 12 which have a shearing value of 21.11 μsec.

The calculated 3QMAS efficiency with quadrupolar coupling constant (C_q) in Lee *et al.* (2010) was used for the calibration. The calibration factors obtained were 7.9 for $^{[4]}$Al, 9.3 for $^{[5]}$Al, and 10.8 for $^{[6]}$Al, respectively. The fractions obtained from 1D isotropic projections were divided by the calibration factor for each site, yielding the final fraction of each peak. The calibrated fractions for $^{[4]}$Al, $^{[5]}$Al, and $^{[6]}$Al in sol-gel synthesized Al_2O_3 are 42.0%, 45.8%, and 12.2%. (The fractions were also calculated by planimetry on the 2D 3QMAS NMR spectra and the calibrated fractions for $^{[4]}$Al, $^{[5]}$Al, and $^{[6]}$Al are 48.1%, 43.7%, and 8.3%).

Figure 14 shows the population of $^{[5]}$Al in Al_2O_3 with annealing time which was calculated with Gaussian fitting of isotropic projections and calibrated. The population of $^{[5]}$Al in samples annealed at 1073 K changes from ~45% to ~0% for 30 min and the population of $^{[5]}$Al in samples annealed at 973 K changes from ~45% to ~32% for 30 min and to ~18% for 120 min. There seems to be two

different rate regions in structural transitions of Al_2O_3 which are the faster transition region in the early stage and the slower transition region in the late stage of structural transitions.

Figure 18 shows the simulated functions for the relationship between time and fractional changes of $^{[5]}Al$ in Al_2O_3 annealed at 1073 K. $\boldsymbol{X_{Al\text{-}5}(t)}$ is defined as the ratio of the population of $^{[5]}Al$ at time $\boldsymbol{t}$ to the initial population of $^{[5]}Al$ in sol-gel synthesized Al_2O_3 (45.8%). In the red region ($0 \le t \le 6.7$ min), the data follows the equation $\boldsymbol{X_{Al\text{-}5}(t)} = exp\ (- 0.053\ t\ )$. In the blue region ($t \ge 6.7$ min), the relationship is $\boldsymbol{X_{Al\text{-}5}(t)} = 0.7\ exp\ (- 3.5 \times 10^{-6}\ t^4\ )$. This relation follows JMA equation ($\boldsymbol{X_{Al\text{-}5}(t)}$ is equivalent to **"1-X"** in **E**q. 4). The constant 0.7 (= exp (-5.3 x 10^{-2} x 6.7)) and t_1 = 6.7 min were set as the fraction when the glass to crystal transition started to be observable by prediction from XRD patterns where the sharp peak is shown (Figure 15).

Figure 19 shows the relationship between annealing time and fractional changes of $^{[5]}Al$ in Al_2O_3 at 973 K. Data points are simulated by using exponential functions. In the red region ($0 \le t \le 14.1$ min), the data follows the equation $\boldsymbol{X_{Al\text{-}5}(t)} = exp\ (- 0.025\ t\ )$. In the blue region ($t \ge 14.1$ min), the relationship is $\boldsymbol{X_{Al\text{-}5}(t)} = 0.7\ exp\ (- 3.5 \times 10^{-9}\ t^4\ )$. The constant 0.7 were set as Figure 17 and t_1 (=14.1 min) is calculated from the equation $0.7 = exp\ (-0.025\ t_1)$.

Figure 21 illustrates the population of $^{[5]}Al$ in Al_2O_3 with annealing temperature. It suggests the crystallization is the process occurring when the structure is activated.

3.3.3. Powder X-ray diffraction

Powder X-ray diffraction spectra were collected on a X-ray diffractometer in continuous mode between 2θ values of 10˚ and 70˚, with a step size 0.02˚/s and scan speed 0.3s. Figure 15 shows the X-ray diffraction (XRD) patterns of amorphous Al_2O_3 and Al_2O_3 samples annealed for 1, 3, 5, 10, 20 and 120 min at 1073 K. The indexed miller indices on the peaks are for γ-Al_2O_3 and the Al_2O_3 samples annealed at 1073 K for 30 min and 2 h show the features of γ-Al_2O_3. As synthesized and 1 and 5 min annealing Al_2O_3 show the broad diffraction patterns for amorphous materials. Sharp peaks at 45° and 66° appear for the 10 min and 20 min annealing which is not γ-Al_2O_3 but the phase with a detectable degree of partial crystallization.

Figure 16 shows the X-ray diffraction (XRD) patterns of Al_2O_3 samples annealed for 2 h at different temperatures (873 K, 973 K, 1038 K, and 1073 K). Partially crystallized phases of samples annealed for 10 min and 20 min in Figure 15 cannot be shown in these temperature settings. There seems to be abrupt changes in structures between 873 K and 973 K annealing samples which overcome the activation energy for crystallization.

3.3.4. TEM analysis

TEM (Transmission electron microscope) images and electron diffraction patterns (SAED) were obtained in a FEI Tecnai F20 TEM under 200 kV of acceleration voltage condition. Figure 17 shows the TEM image of amorphous

and crystallized Al_2O_3. Figure 17(A) is the image of Al_2O_3 annealed for 5 min at 1073 K. There is a 1~3 nm density fluctuation, indicating the sample could be porous. The SAED pattern shows the typical feature of amorphous materials. Figure 17(B) is the image of Al_2O_3 annealed for 60 min at 1073 K. Black lumpy area seems crystallized and the SAED of the black area shows the scattering ring and diffraction points which indicate the existence of crystals with a high structural disorder. This corresponds to the TEM study of γ-alumina(Chou *et al.*, 1991). These TEM results confirm the absence of crystallinity in the red region but crystalline phases observable in the blue region (in Figure 18).

3.3.5. Discussion

1D MAS NMR and 2D 3QMAS NMR results show the effect of temperature and time on structural transitions in alumina. Well-resolved Al-coordination environments have revealed the mechanism related to the annihilation of $^{[5]}Al$ during the transformation of amorphous Al_2O_3 to crystalline Al_2O_3 which can be described by the following scheme: $2\,^{[5]}Al \rightarrow {}^{[4]}Al + {}^{[6]}Al$, as reported in Lee *et al.* (2009).

The fraction of $^{[5]}Al$ could be a good proxy for the degree of structural transitions such as crystallization processes. In Figure 17 and 18, the equation to show the degree of transitions was simulated by exponential functions. When t is smaller than t_1 (the time that the glass to crystal transition starts to be observed), glass-glass transition (structural transitions within glass) is dominant and the

degree of transitions in Al_2O_3 follows $\mathbf{X_{Al\text{-}5}}$ (t) = exp (- k_1 t). When *t* is larger than t_1, glass-crystal transition (crystallization) is dominant and $\mathbf{X_{Al\text{-}5}}$ (t) = *exp* (- k_1 t_1) [*exp* (- k_2 t^4) + { 1- *exp* (- k_2 t^4)} *exp* (- k_3 t)]. In this system, the mechanism related to annihilation of $^{[5]}$Al is mostly glass-glass transition and glass-crystal transition and thus the effect of crystal-crystal transition part ({1- *exp* (- k_2 t^4)} *exp* (- k_3 t)) can be ignored.

Upon simulating $^{[5]}$Al fraction with respect to annealing time and temperature, we obtained rate constants for structural transitions within glass (process 1, k_1) and crystallization of amorphous Al_2O_3 (process 2, k_2) at both 973 and 1073 K. As for the process 1, k_1 increases from 2.5 x 10^{-2} at 973 K to 5.3 x 10^{-2} at 1073 K. As for the crystallization of amorphous oxide, k_2 varies from 3.5 x 10^{-9} (at 973 K) to 3.5 x 10^{-6} (at 1073 K). Activation energy barriers $\boldsymbol{E_a}$ for the two distinct processes responsible for the change in $^{[5]}$Al were obtained from the above Arrhenius plot (Figure 20). Calculated activation energies barrier for processes 1 and 2 are 6.5 x 10 kJ mol^{-1} and 6.0 x 10^2 kJ mol^{-1}, respectively. These results may indicate that the annihilation of $^{[5]}$Al upon crystallization is kinetically hindered while that within amorphous network is kinetically more favored.

We repeated crystallization experiments in order to check the reproducibility. Additional experimental attempt to obtain rate constants for structural transitions within glass and crystallization was conducted. Figure 22, 23 and 24 show the two-dimensional ^{27}Al 3QMAS NMR spectra for Al_2O_3 annealed at 998 K, 1023 K and 1073 K (the second attempt) with varying

annealing time. Total isotropic projections of these spectra are presented in Figure 25, 27 and 29. Figure 26, 28 and 30 show the results of simulation with 3 Gaussian peaks of the rotated total isotropic projection of the ^{27}Al 3QMAS NMR spectra. Isotropic projection spectra have been rotated about 30° clockwise to make spectra more fitted in Gaussian functions (A shearing value has changed 12 μsec from 21.11 μsec). Figure 31, 32, 33 and 34 present the relationship between annealing time and fractional changes of $^{[5]}Al$ in Al_2O_3 annealed at 998 K, 1023 K, 1073 K and all together (the second attempt). The calculated k_1 at 998 K, 1023 K, and 1073 K are 5.2×10^{-4}, 2.3×10^{-3}, and 1.6×10^{-2} and k_2 are 9.3×10^{-14}, 3.2×10^{-11}, and 6.5×10^{-8}, respectively. With these values, activation energies for the two distinct processes were obtained. Figure 35 shows Arrhenius plot for Al_2O_3. Calculated activation energies barrier for processes 1 and 2 are 4.0×10^2 kJ mol^{-1} and 1.6×10^3 kJ mol^{-1}, respectively.

The estimated activation energy for each process is 6 and 2.6 times larger than those from previous results (Figure 20; 6.5 x 10 kJ mol^{-1} for the process 1 and 6.0×10^2 kJ mol^{-1} for the process 2, respectively). Exact origins of this discrepancy is not clear, it may be due to the presence of residual carbon phase (*e.g.*, residual organic ligand) and hydration shell. Indeed, it should be also noted that previous studies on crystallization kinetics have shown that presence of minor impurity or hydration shell can have enormous effect on its activation energy barrier for crystallization. If a heterogeneous surface (impurity) is available, the surface energy of a cluster will reduce. Since the surface energy of the cluster is lower, the critical radius will be smaller and the nucleation rate will be larger (Kirkpatrick, 1981). In addition, the content of volatiles such as H_2O affects

crystallization rate (*e.g.*, Fokin *et al.*, 2006). Since viscosity reduction lowers kinetic barrier, the nucleation rate increases with increasing H_2O contents. The relationship between viscosity and nucleation rate is also described in Eq. 2.

Detailed micro-texture analysis using TEM and phase identification using XRD are certainly necessary to confirm the potential origins of the observed discrepancy. Despite the uncertainty in the estimated activation energy barrier, Figure 35 clearly shows that ln k decreases linearly with increasing 1/T, suggesting that each process can be described with Arrhenius behaviors and the estimated trends are robust.

We also note that the current trend is specific for amorphous Al_2O_3 at 1 atm. Therefore, future studies on crystallization kinetics for diverse amorphous oxides at both ambient and high pressure remains to be explored.

4. Oxygen Triclusters in Amorphous Al_2O_3

4.1. Introduction

In Ca-aluminate melts, anomalous viscos behavior has been reported. This previous macroscopic measurement suggested the presence of oxygen triclusters (oxygen coordinated by three aluminums, $^{[3]}O$) in Al-rich melt at 1 atm. Also, by the molecular dynamics simulations of Al_2O_3 melts, the high $^{[5]}Al$ content in amorphous Al_2O_3 is indicative of a large number of oxygen triclusters (*e.g.*, Jahn and Madden, 2007; Ansell *et al.*, 1997) contradicting the traditional view that oxygen atoms should bond to just two other atoms. Here, we report experimental evidences of oxygen triclusters in amorphous alumina at 1 atm.

4.2. O-17 NMR for amorphous Al_2O_3

In order to confirm the coordination environment of oxygen in amorphous Al_2O_3 by ^{17}O NMR, several ^{17}O enriching experiments were conducted. At first, amorphous Al_2O_3 was sol-gel synthesized by dissolving aluminum L-lactate in ^{17}O enriched water ($H_2{}^{17}O$). However, the enrichment level was quite low to obtain high resolution NMR signals. For the higher enrichment level, the hydrothermal experiment on sol-gel synthesize Al_2O_3 at 500 bar and 673 K was conducted, but it produced crystalline Al_2O_3 with only $^{[6]}Al$. With $^{17}O_2$ gas

exchange experiments on sol-gel synthesized Al_2O_3, we finally obtained the successful NMR results.

Figure 36 shows ^{17}O MAS NMR spectra for sol-gel synthesized Al_2O_3 (black) compared to those of γ-Al_2O_3 (blue) and Na-aluminosilicate glass (red). The oxygen coordination environment of amorphous Al_2O_3 is characterized with mostly $^{[3]}O$ and a small fraction of $^{[2,4]}O$. This species distribution is similar to previous results of molecular dynamics simulations. Jahn (2008) reported the mean coordination number of pure Al_2O_3 is 2.94 and 75% of the O are surrounded by 3 Al ions. Figure 37 presents ^{17}O 3QMAS NMR spectra for sol-gel synthesized Al_2O_3 (left) and γ-Al_2O_3 (right). The larger fractions of $^{[2,3]}O$ are existent in amorphous Al_2O_3 than crystalline phase. These results are the first experimental evidences of the existence of $^{[3]}O$ in amorphous Al_2O_3 at 1 atm revealed by ^{17}O MAS & 3QMAS NMR.

4.3. Quantum simulation

Quantum chemical calculations using Gaussian 03 (Foresman *et al.,* 1996) were performed to find NMR parameters for oxygen triclusters in amorphous Al_2O_3. Clusters were constructed with central $^{[3]}O$ connected by 2 of $^{[5]}Al$ and 1 $^{[4]}Al$ and 3 $^{[5]}Al$. Figure 38(A) and Figure 39(A) show atomistic models for amorphous Al_2O_3 clusters built as starting structures for calculations. These clusters were optimized with the B3LYP hybrid density functional theory and the 6-311+G(2d,p) basis set. However, the present study failed to optimize the

structure of clusters as shown in Figure 38(B) and Figure 39(B). Oxygen triclusters are seemed unstable because they were the bond broken through optimization process. The suitable network surrounding the $^{[3]}O$ is in need for the existence of $^{[3]}O$.

5. Future Studies

The nature of silicate melts at high pressure and temperature governs magmatic processes in the Earth's interior. And it probably dominated the differentiation of Earth in the Hadean magma ocean where significant fractions of the Earth were melts (Ohtani, 1985; Tonks and Melosh, 1993; Labrosse *et al.*, 2007). Even though the kinetics of crystallization in melts at 1 atm was revealed, the phase relation in the deep magma ocean (*i.e.*, at high pressure) could be different. Therefore studies on crystallization processes at high pressure will be necessary to confirm the current discussions and to shed more light on the deep magma ocean and mantle.

Especially the structural evolution of basaltic melts and glasses is essential to understand not only the chemical differentiation of the early Earth but also geochemical processes involving magmas. Because of difficulties in experimental analysis by a compositional complexity, however, it has not been well known. Recently, Park and Lee (2012) reported the effects of composition on the structural changes in the CMAS glasses with improved 3QMAS NMR techniques. Effects of time and temperature are not explored yet, but it is worth to study them in basaltic melts at various pressure conditions to have better understanding about crystallization of magma ocean.

6. Conclusion

In order to have better insights into the chemical differentiation of Earth from its magma ocean phase to the current stratified structure, detailed information of crystallization kinetics of silicate melts consisting of the magma ocean is essential. The structural transitions in oxide glasses and melts upon crystallization provide improved prospects for a systematic and quantitative understanding of the crystallization processes.

Here, we reported the detailed Al-27 MAS and 3QMAS NMR study for the sol-gel synthesized Al_2O_3 glass with varying temperature and annealing time. The NMR spectra for the amorphous Al_2O_3 show well-resolved Al coordination environments, characterized with mostly $^{[4,5]}$Al and a minor fraction of $^{[6]}$Al. The fraction of $^{[5]}$Al in the alumina phase decreases with increasing annealing time at constant temperature. The results also reveal two distinct processes involving annihilation of $^{[5]}$Al, namely structural transitions within glasses with varying degrees of disorder and crystallization into γ-Al_2O_3. Upon simulating $^{[5]}$Al fraction with respect to annealing time and temperature, we obtained the activation energy barriers for structural transitions within glass and crystallization of amorphous Al_2O_3. The results may indicate that the annihilation of $^{[5]}$Al upon crystallization is kinetically hindered while that within amorphous network is kinetically more favored. In this study, it was also found that the estimated activation energy for each process may depend on the presence of

potential residual carbon phases (*e.g.*, residual organic ligand) and presence of hydration shell as has been suggested from the previous studies on crystallization kinetics. Despite uncertainty in the estimated activation energy barrier, ln k decreases linearly with increasing 1/T, suggesting that each process can be described with Arrhenius behaviors.

The current results highlight the first detailed estimation of crystallization kinetics of the archetypal Al_2O_3 on the basis of its atomic scale structural evolution. Additionally, the experimental results, for the first time, revealed the presence of two distinct mechanisms for structural rearrangement upon crystallization in the prototypical single-component oxide glasses. The current results and method can shed light on a new opportunity to study crystallization kinetics of diverse natural and multi-component silicate glasses and melts. The potential result may yield atomic-level understanding of Earth's chemical evolution.

References

Ansell, S., S. Krishnan, J. K. R. Weber, J. J. Felten, P. C. Nordine, M. A. Beno, D. L. Price and M. L. Saboungi (1997) "Structure of liquid aluminum oxide." *Physical Review Letters* **78**(3): 464-466.

Avrami, M. (1941) "Granulation, Phase Change, and Microstructure Kinetics of Phase Change. III." *The Journal of Chemical Physics* **9**(2): 177-184.

Baltisberger, J. H., Z. Xu, J. F. Stebbins, S. H. Wang and A. Pines (1996) "Triple-Quantum Two-Dimensional 27Al Magic-Angle Spinning Nuclear Magnetic Resonance Spectroscopic Study of Aluminosilicate and Aluminate Crystals and Glasses." *Journal of the American Chemical Society* **118**(30): 7209-7214.

Chou, T. C., D. Adamson, J. Mardinly and T. G. Nieh (1991) "Microstructural Evolution and Properties of Nanocrystalline Alumina Made by Reactive Sputtering Deposition." *Thin Solid Films* **205**(2): 131-139.

Davis, M. J. and P. D. Ihinger (2002) "Effects of thermal history on crystal nucleation in silicate melt: Numerical simulations." *Journal of Geophysical Research* **107**(B11): 2284.

Dingwell, D. B. and S. L. Webb (1989) "Structural relaxation in silicate melts and non-Newtonian melt rheology in geologic processes." *Physics and Chemistry of Minerals* **16**: 508-516.

Fokin, V. M., E. D. Zanotto, N. S. Yuritsyn and J. W. P. Schmelzer (2006) "Homogeneous crystal nucleation in silicate glasses: A 40 years perspective." *Journal of Non-Crystalline Solids* **352**: 2681-2714.

Foresman, J. B., A. E. Frisch and I. Gaussian (1996) "Exploring chemistry with electronic structure methods."

Frydman, L. and J. S. Harwood (1995) "Isotropic spectra of half-integer quadrupolar spins from bidimensional magic-angle spinning NMR." *Journal of the American Chemical Society* **117**: 5367-5368.

Gaudio, S. J., S. Sen and C. E. Lesher (2008) "Pressure-induced structural changes and densification of vitreous MgSiO3." *Geochimica Et Cosmochimica Acta* **72**(4): 1222-1230.

Gibson, M. A. and G. W. Delamore (1987) "Crystallization kinetics of some iron-based metallic glasses." *Journal of Materials Science* **22**: 4550-4557.

Hammer, J. E. (2008) Experimental Studies of the Kinetics and Energetics of Magma Crystallization. Minerals, Inclusions and Volcanic Processes. K. D. Putirka and F. J. Tepley. Chantilly, Mineralogical Soc Amer. **69:** 9-59.

Huggins, B. A. and P. D. Ellis (1992) "Aluminum-27 nuclear magnetic resonance study of aluminas and their surfaces." *Journal of the American Chemical Society* **114**(6): 2098-2108.

Jahn, S. and P. A. Madden (2007) "Structure and dynamics in liquid alumina: Simulations with an ab initio interaction potential." *Journal of Non-Crystalline Solids* **353**(32–40): 3500-3504.

Jahn, S. (2008) "Atomic structure and transport properties of MgO-Al_2O_3 melts: A molecular dynamics simulation study." *American Mineralogist* **93**(10): 1486-1492.

James, P. F. (1974) "Kinetics of crystal nucleation in lithium silicate glasses." *Physics and Chemistry of Glasses* **15**: 95-105.

James, P. F. (1985) "Kinetics of crystal nucleation in silicate glasses." *Journal of Non-Crystalline Solids* **73**: 517-540.

Johnson, W. A. and R. F. Mehl (1939) "Reaction kinetics in processes of nucleation and growth." *Transactions of the American Institute of Mining and Metallurgical Engineers* **135**: 416-442.

Kelton, K. F. and A. L. Greer (1988) "Test of classical nucleation theory in a condensed system." *Physical Review B* **38**(14): 10089-10092.

Kelton, K. F. and A. L. Greer (2010) CHAPTER 8 - Crystallization in Glasses. Pergamon Materials Series. K. F. Kelton and A. L. Greer, Pergamon. Volume **15:** 279-329.

Kingery, W. D., H. K. Bowen and D. R. Uhlmann (2006) Introduction to Ceramics. New York, John Wiley & Sons.

Kirkpatrick, R. J. (1981) Kinetics of crystallization of igneous rocks. Kinetics of geochemical processes, Reviews in mineralogy. A. C. a. K. Lasaga, R.J., Mineralogical Society of America. **8:** 321-398.

Kissinger, H. E. (1957) "Reaction Kinetics in Differential Thermal Analysis." *Analytical Chemistry* **29**(11): 1702-1706.

Kooi, B. J., W. M. G. Groot and J. T. M. De Hosson (2004) "In situ transmission electron microscopy study of the crystallization of $Ge_2Sb_2Te_5$." *Journal of Applied Physics* **95**(3): 924-932.

Lee, S. K. (2004) "Structure of Silicate Glasses and Melts at High Pressure: Quantum Chemical Calculations and Solid-State NMR." *The Journal of Physical Chemistry B* **108**(19): 5889-5900.

Lee, S. K. (2011) "Simplicity in melt densification in multicomponent magmatic reservoirs in Earth's interior revealed by multinuclear magnetic resonance." *Proceedings of the National Academy of Sciences* **108**(17): 6847-6852.

Lee, S. K., G. D. Cody, Y. W. Fei and B. O. Mysen (2004) "Nature of polymerization and properties of silicate melts and glasses at high pressure." *Geochimica Et Cosmochimica Acta* **68**(20): 4189-4200.

Lee, S. K., S. B. Lee, S. Y. Park, Y. S. Yi and C. W. Ahn (2009) "Structure of Amorphous Aluminum Oxide." *Physical Review Letters* **103**(9): 095501.

Lee, S. K., J. F. Lin, Y. Q. Cai, N. Hiraoka, P. J. Eng, T. Okuchi, H. K. Mao, Y. Meng, M. Y. Hu, P. Chow, J. F. Shu, B. S. Li, H. Fukui, B. H. Lee, H. N. Kim and C. S. Yoo (2008) "X-ray Raman scattering study of $MgSiO_3$ glass at high pressure: Implication for triclustered MgSiO3 melt in Earth's mantle." *Proceedings of the National Academy of Sciences of the United States of America* **105**(23): 7925-7929.

Lee, S. K., C. B. Musgrave, P. Zhao and J. F. Stebbins (2001) "Topological Disorder and Reactivity of Borosilicate Glasses: Quantum Chemical Calculations and ^{17}O and ^{11}B NMR Study." *The Journal of Physical Chemistry B* **105**(50): 12583-12595.

Lee, S. K., S. Y. Park, Y. S. Yi and J. Moon (2010) "Structure and Disorder in Amorphous Alumina Thin Films: Insights from High-Resolution Solid-State NMR." *Journal of Physical Chemistry C* **114**(32): 13890-13894.

Lee, S. K. and J. F. Stebbins (2000) "The Structure of Aluminosilicate Glasses: High-Resolution ^{17}O and ^{27}Al MAS and 3QMAS NMR Study." *The Journal of Physical Chemistry B* **104**(17): 4091-4100.

Lee, S. K. and J. F. Stebbins (2002) "Extent of intermixing among framework units in silicate glasses and melts." *Geochimica Et Cosmochimica Acta* **66**(2): 303-309.

Lee, S. K. and J. F. Stebbins (2006) "Disorder and the extent of polymerization in calcium silicate and aluminosilicate glasses: O-17NMR results and

quantum chemical molecular orbital calculations." *Geochimica Et Cosmochimica Acta* **70**(16): 4275-4286.

Lee, S. K. and J. F. Stebbins (2009) "Effects of the degree of polymerization on the structure of sodium silicate and aluminosilicate glasses and melts: An 17O NMR study." *Geochimica Et Cosmochimica Acta* **73**(4): 1109-1119.

Levitt, M. H. (2008) Spin dynamics : Basic of Nuclear Magnetic Resonance. Chichester, John Wiley & Sons Ltd.

Murakami, M. and J. D. Bass (2011) "Evidence of denser $MgSiO_3$ glass above 133 gigapascal (GPa) and implications for remnants of ultradense silicate melt from a deep magma ocean." *Proceedings of the National Academy of Sciences of the United States of America* **108**(42): 17286-17289.

Ohtani, E. (1985) "The primodial terrestrial magma ocean and its implication for stratification of the mantle." *Physics of the Earth and Planetary Interiors* **38**(1): 70-80.

Park, S. Y. and S. K. Lee (2012) "Structure and disorder in basaltic glasses and melts: Insights from high-resolution solid-state NMR study of glasses in diopside–Ca-tschermakite join and diopside–anorthite eutectic composition." *Geochimica Et Cosmochimica Acta* **80**(0): 125-142.

Ree, T. and H. Eyring (1958) The relaxation theory of transport phenomena. Rheology: Theory and Applications. F. R. Eirich. New York, Academic Press. **2**.

Richerson, D. W. (1992) Modern Ceramic Engineering, Marcel Dekker Inc.

Rosenflanz, A., M. Frey, B. Endres, T. Anderson, E. Richards and C. Schardt (2004) "Bulk glasses and ultrahard nanoceramics based on alumina and rare-earth oxides." *Nature* **430**(7001): 761-764.

Scott, M. G. (1983) Crystallization. Amorphous Metallic Alloys. F. E. Luborsky. London, Butterworths**:** 144–168.

Shelby, J. E. (1997) Introduction to glass science and technology, The Royal Society of Chemistry.

Solomatov, V. (2007) Magma Oceans and Primordial Mantle Differentiation. Treatise on Geophysics. S. Editor-in-Chief: Gerald. Amsterdam, chapter 9.04, Elsevier**:** 91-119.

Stebbins, J. F., S. Kroeker, S. K. Lee and T. J. Kiczenski (2000) "Quantification of five- and six-coordinated aluminum ions in aluminosilicate and fluoride-containing glasses by high-field, high-resolution 27Al NMR." *Journal of Non-Crystalline Solids* **275**(1–2): 1-6.

Stixrude, L. and B. Karki (2005) "Structure and Freezing of $MgSiO_3$ Liquid in Earth's Lower Mantle." *Science* **310**(5746): 297-299.

Tonks, W. B. and H. J. Melosh (1993) "Magma Ocean Formation Due to Giant Impacts." *Journal of Geophysical Research* **98**(E3): 5319-5333.

Toplis, M. J., S. C. Kohn, M. E. Smith and I. J. F. Poplett (2000) "Fivefold-coordinated aluminum in tectosilicate glasses observed by triple quantum MAS NMR." *American Mineralogist* **85**(10): 1556-1560.

Turnbull, D. and M. Cohen (1960) Crystallization kinetics and glass formation. Modern Aspects of the Vitreous State. J. D. MacKenzie. London, Butterworth and Co.**:** 38-62.

Wuttig, M. and N. Yamada (2007) "Phase-change materials for rewriteable data storage." *Nature Materials* **6**(11): 824-832.

Zhang, H. and J. F. Banfield (2002) "Kinetics of crystallization and crystal growth of nanocrystalline anatase in nanometer-sized amorphous titania." *Chemistry of Materials* **14**: 4145-4154.

Zhang, L., J. C. C. Chan, H. Eckert, G. Helsch, L. P. Hoyer and G. H. Frischat (2003) "Novel sol-gel synthesis of sodium aluminophosphate glass based on aluminum lactate." *Chemistry of Materials* **15**(14): 2702-2710.

Zhang, L., C. C. de Araujo, and H. Eckert (2007) "Aluminum lactate - An attractive precursor for sol-gel synthesis of alumina-based glasses." *Journal of Non-Crystalline Solids* **353**(13-15): 1255-1260.

Zhang, L. and H. Eckert (2004) "Multinuclear NMR studies on the sol-gel preparation of sodium aluminophosphate glasses." *Solid State Nuclear Magnetic Resonance* **26**(3-4): 132-146.

Zhang, L. and H. Eckert (2005) "Synthesis and structural evolution of Al_2O_3-B_2O_3-P_2O_5 gels and glasses." *Journal of Materials Chemistry* **15**(16): 1640-1653.

Figures

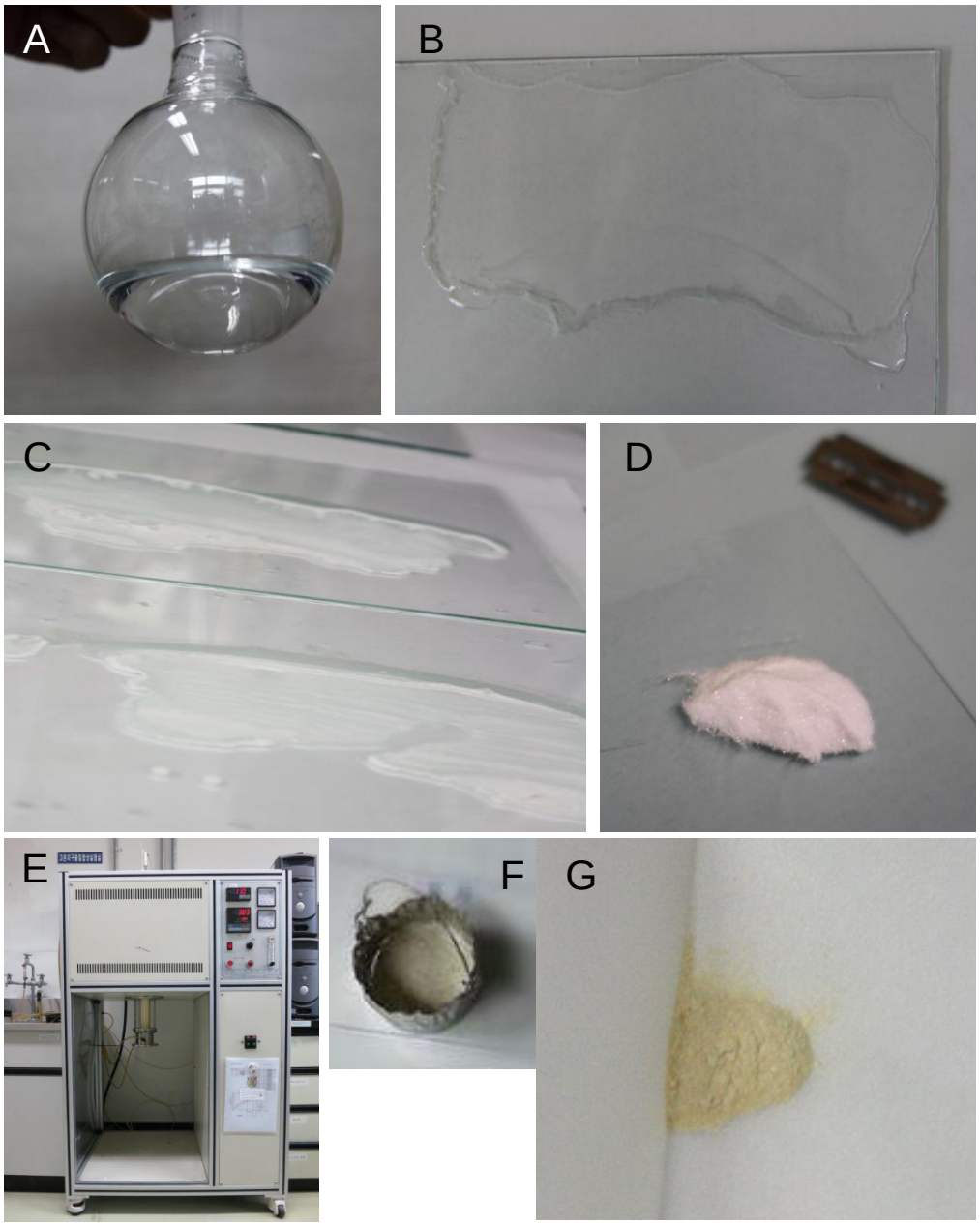

Figure 1| Sample synthesis procedure of amorphous Al_2O_3 by sol-gel method.

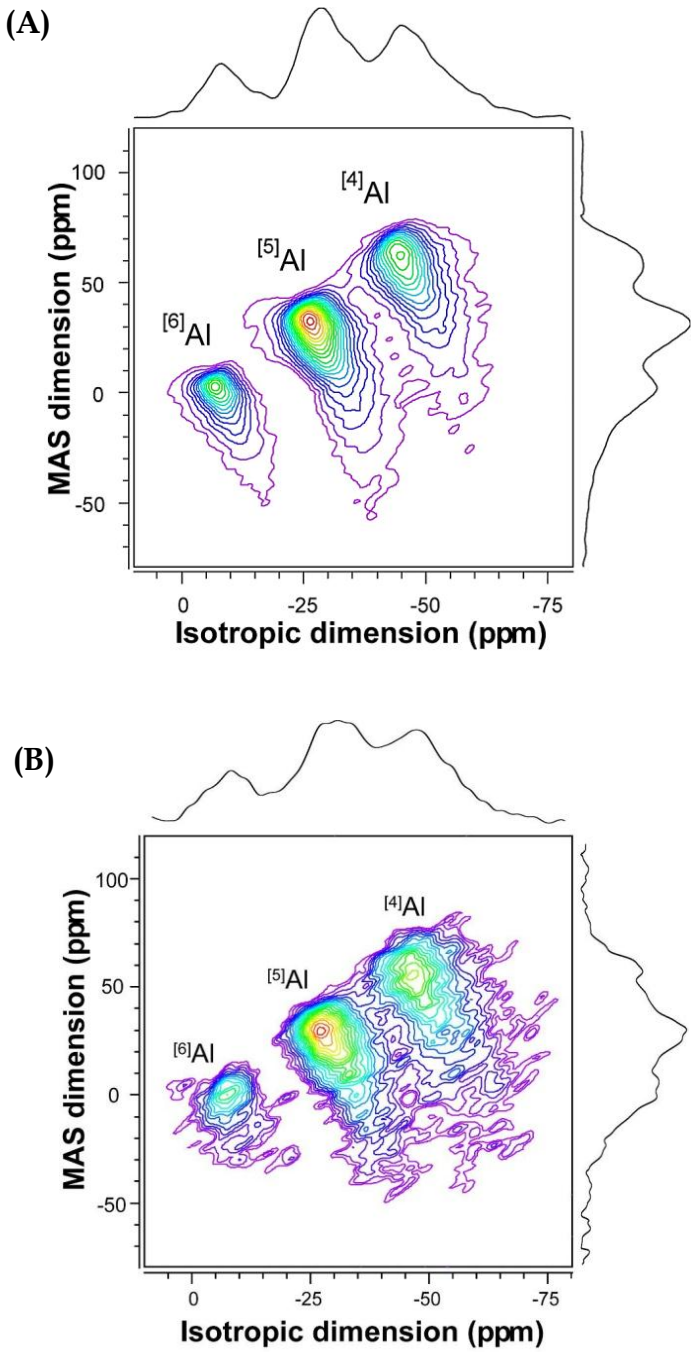

Figure 2| ^{27}Al 3QMAS NMR spectra for (A) sol-gel synthesized Al_2O_3 and (B) amorphous Al_2O_3 thin film (Lee et al., 2009).

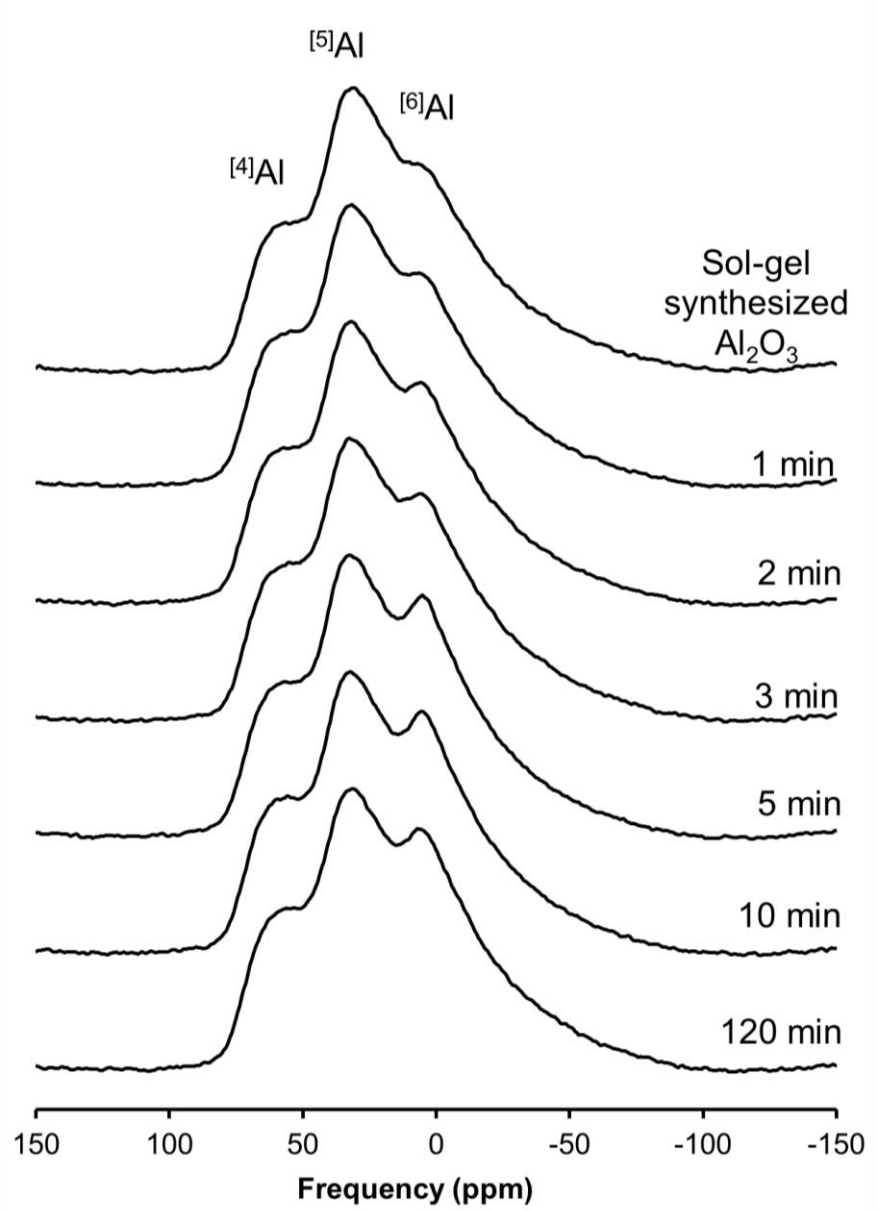

Figure 3 | ^{27}Al MAS NMR spectra for Al_2O_3 annealed at 896 K for 1, 2, 3, 5, 10 and 120 min.

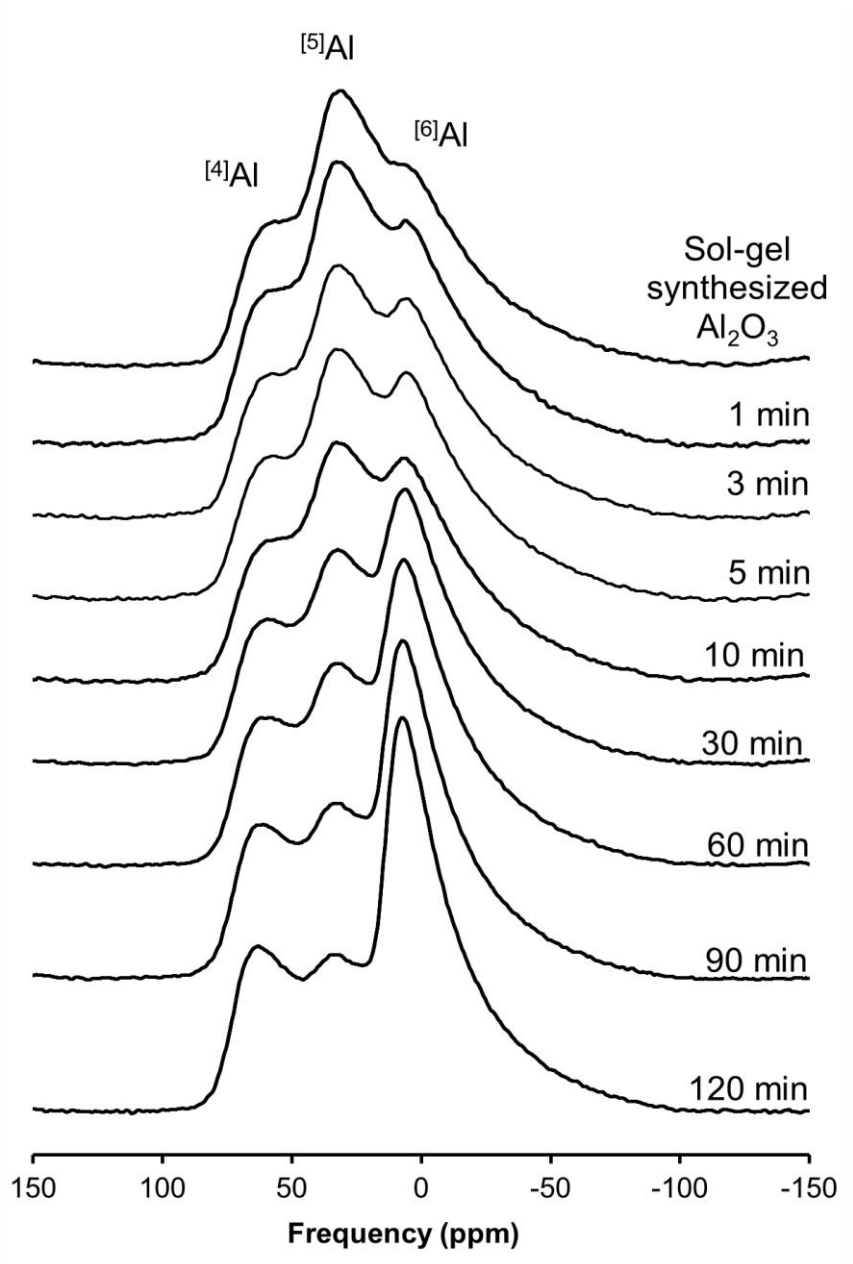

Figure 4 | ^{27}Al MAS NMR spectra for Al_2O_3 annealed at 973 K for 1, 3, 5, 10, 30, 60, 90 and 120 min.

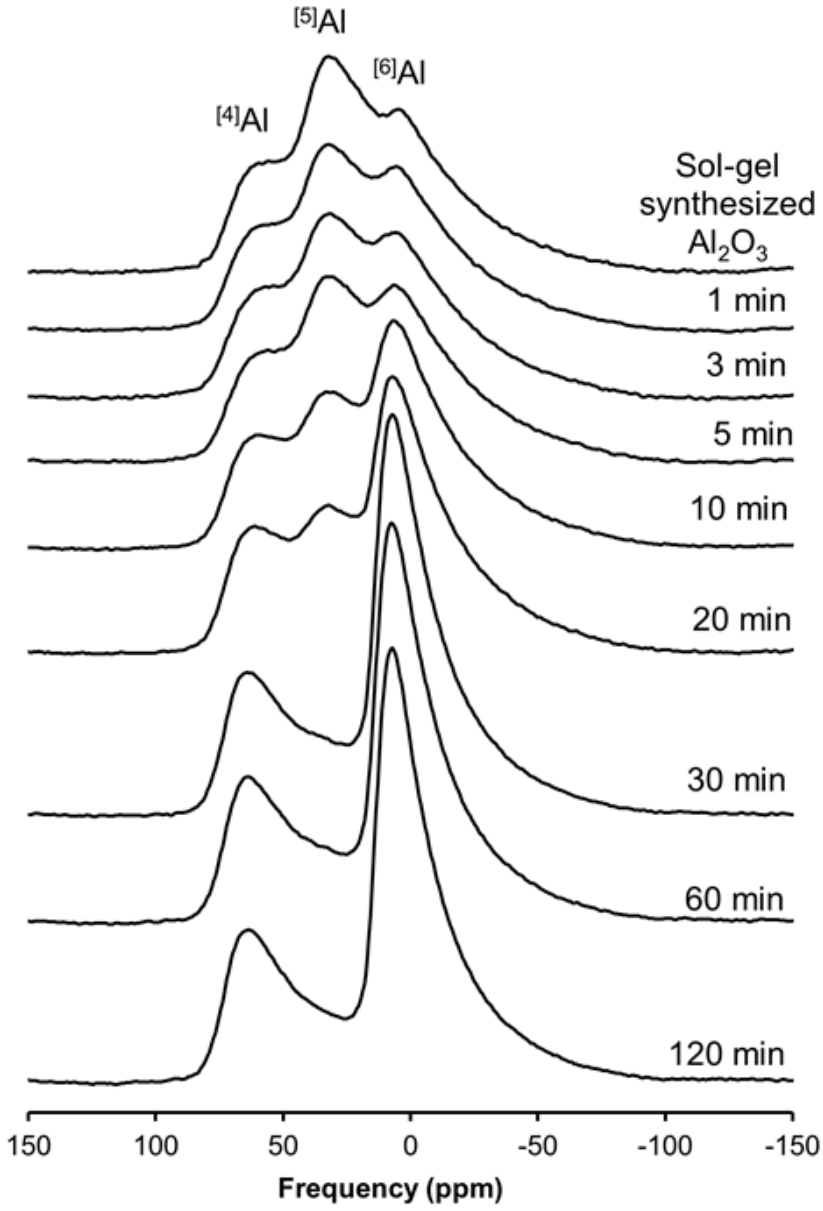

Figure 5 | ^{27}Al MAS NMR spectra for Al_2O_3 annealed for 1, 3, 5, 10, 20, 30, 60 and 120 min at 1073 K.

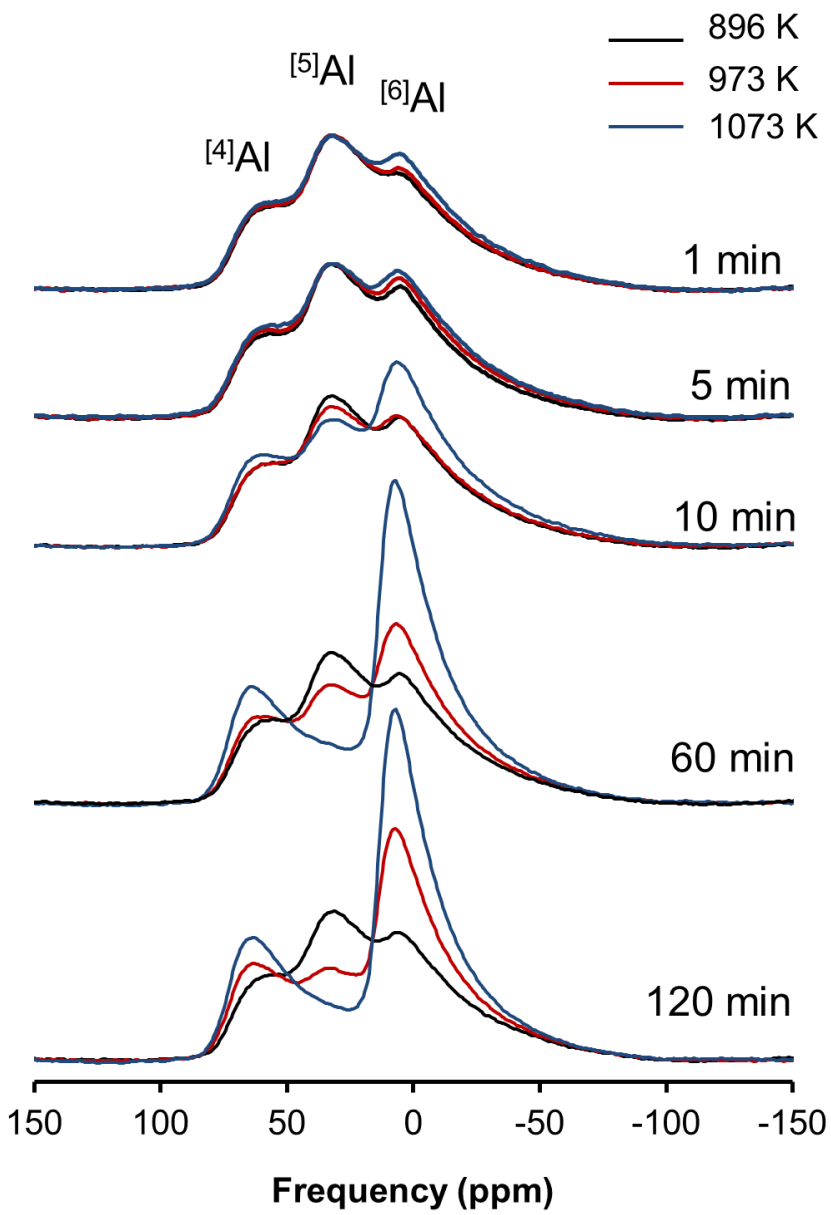

Figure 6| ^{27}Al MAS NMR spectra for Al_2O_3 annealed for 1, 5, 10, 60 and 120 min at 896 K, 973 K and 1073 K.

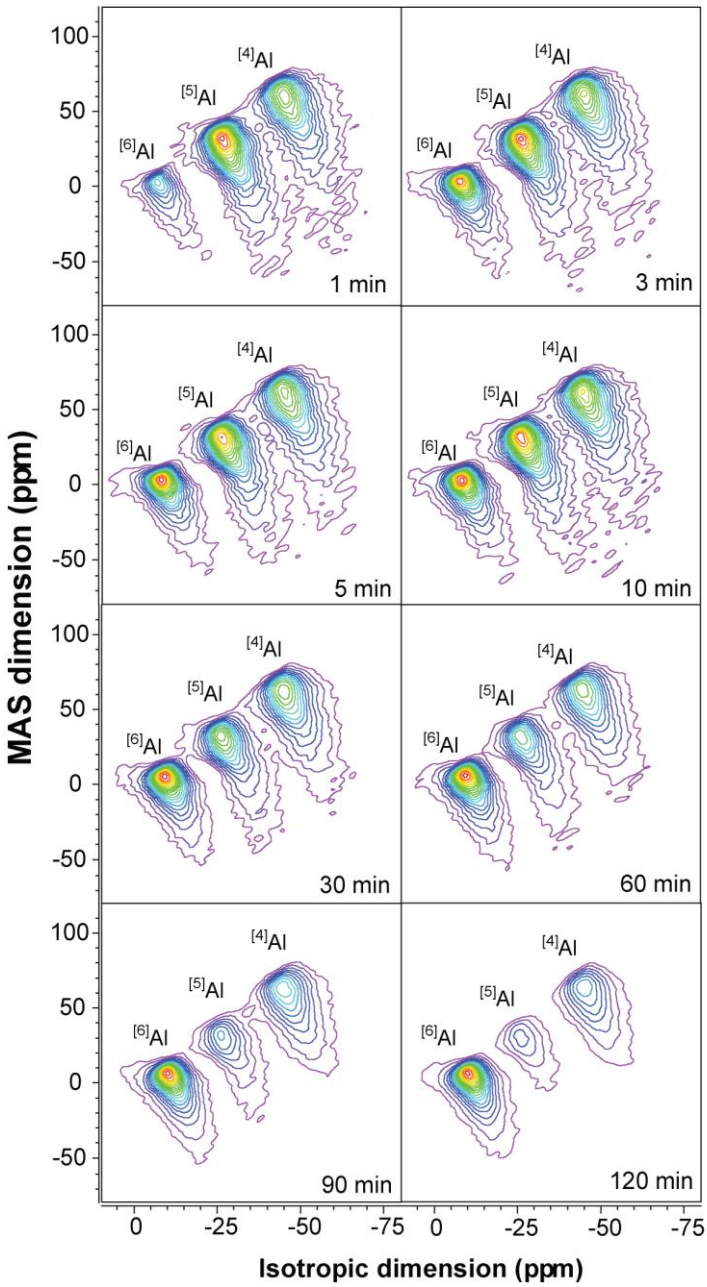

Figure 7| ^{27}Al 3QMAS NMR spectra for Al_2O_3 annealed at 973 K with varying annealing time. Contour lines are drawn at 5% intervals from relative intensities of 8% to 98% with an added line at 4%.

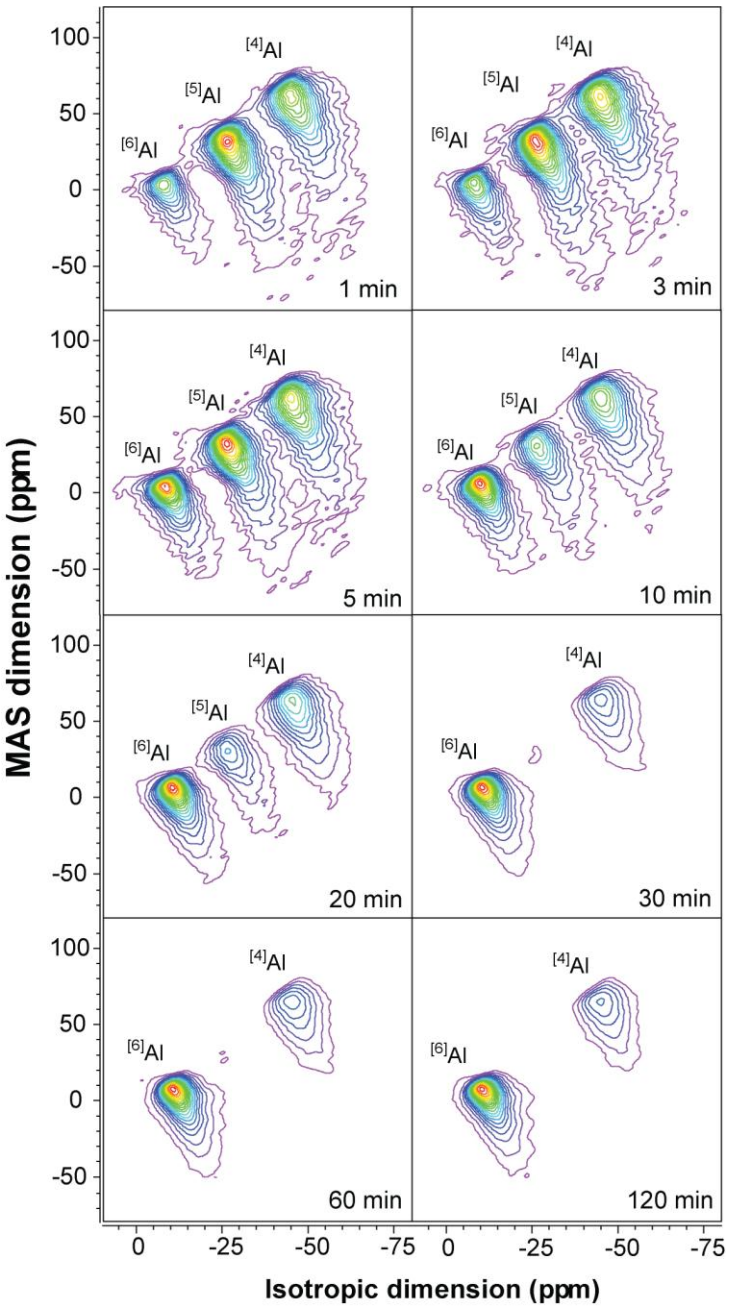

Figure 8 | ^{27}Al 3QMAS NMR spectra for Al_2O_3 annealed at 1073 K with varying annealing time. Contour lines are drawn at 5% intervals from relative intensities of 8% to 98% with an added line at 4%.

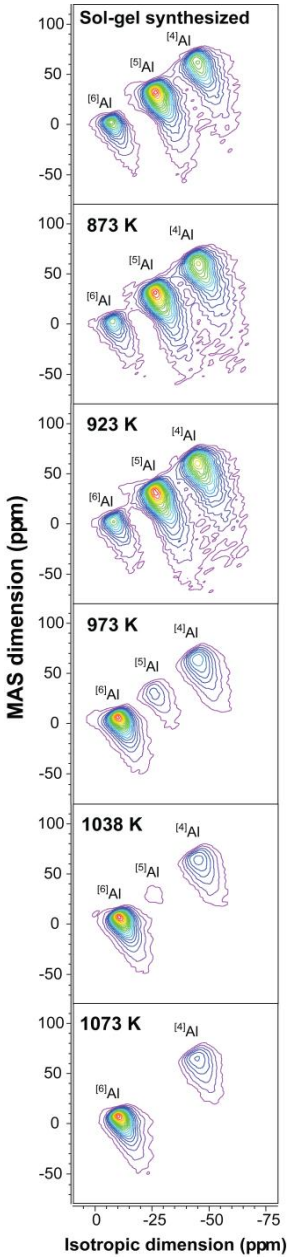

Figure 9 | ^{27}Al 3QMAS NMR spectra for Al_2O_3 annealed for 2 h at 873 K, 923 K, 973 K, 1038 K and 1073 K. Contour lines are drawn at 5% intervals from relative intensities of 8% to 98% with an added line at 4%.

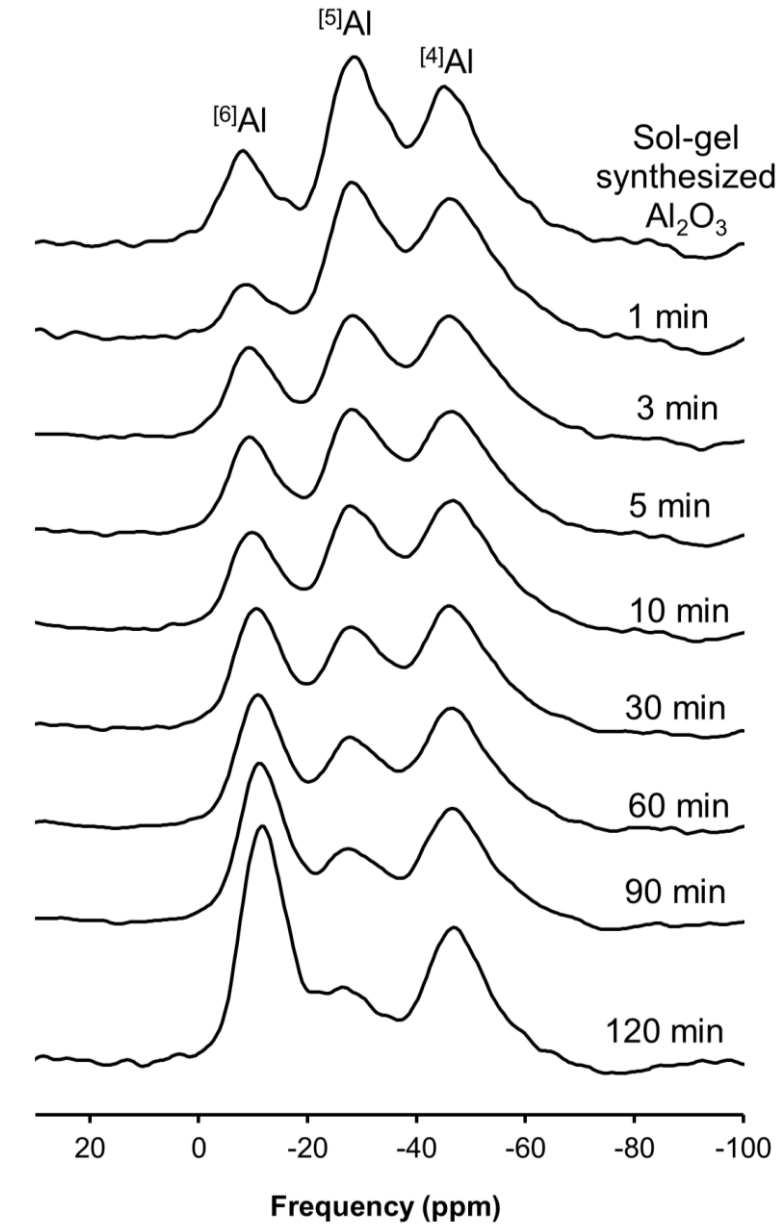

Figure 10| Total isotropic projections of ^{27}Al 3QMAS NMR spectra for Al_2O_3 annealed at 973 K with varying annealing time.

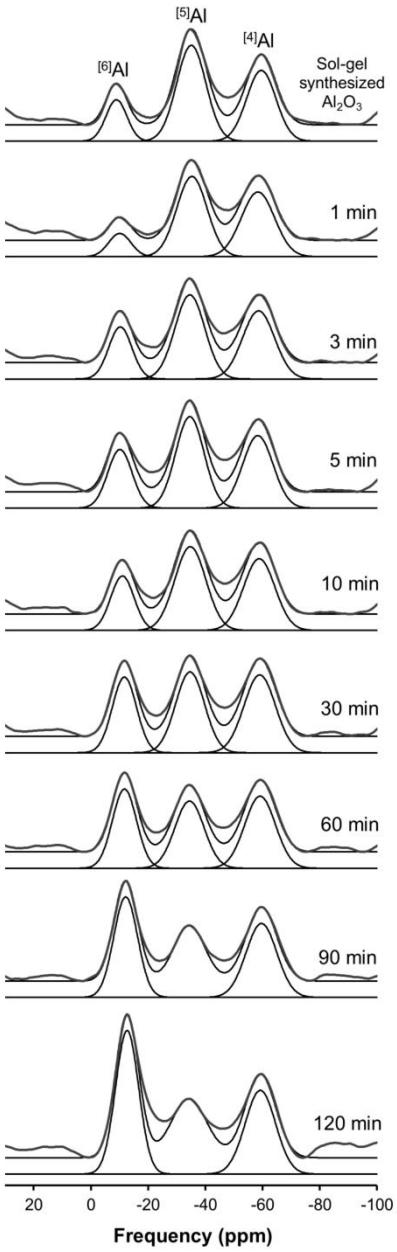

Figure 11| Results of simulating Gaussian functions (black lines) of isotropic projections of the ^{27}Al 3QMAS NMR spectra for Al_2O_3 annealed at 973 K with varying annealing time. The gray lines refer to the experimental spectra rotated 30º clockwise.

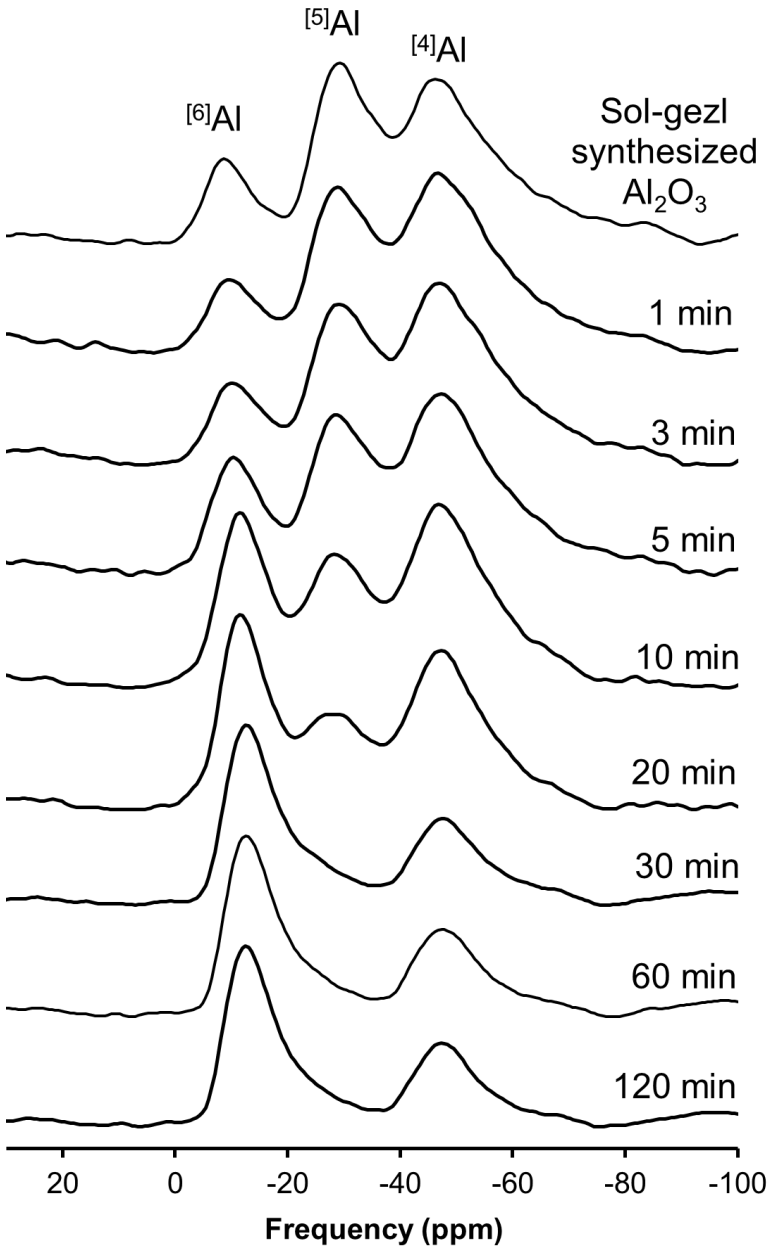

Figure 12| Total isotropic projections of ^{27}Al 3QMAS NMR spectra for Al_2O_3 annealed at 1073 K with varying annealing time.

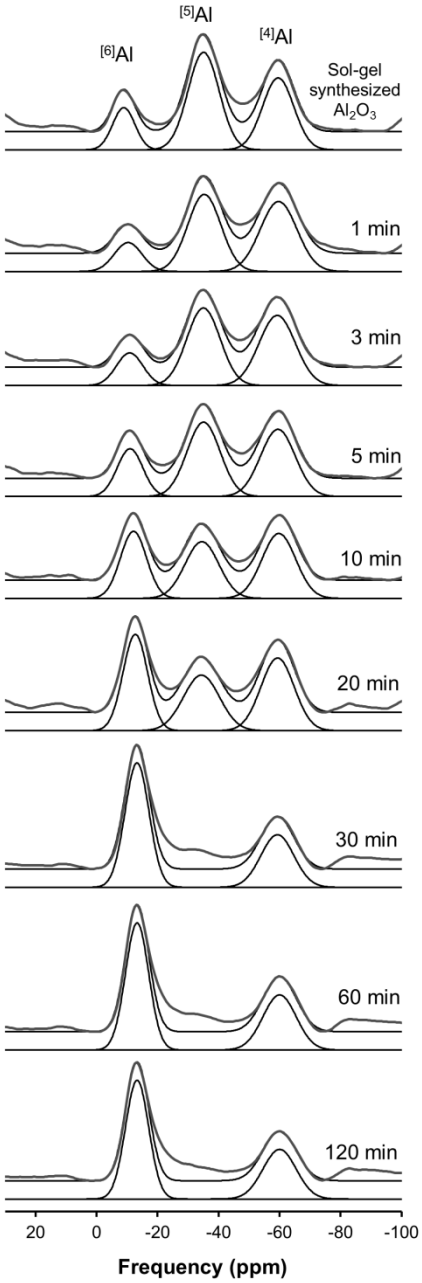

Figure 13| Results of simulating Gaussian functions (black lines) of isotropic projections of the ^{27}Al 3QMAS NMR spectra for Al_2O_3 annealed at 1073 K with varying annealing time. The gray lines refer to the experimental spectra rotated 30º clockwise.

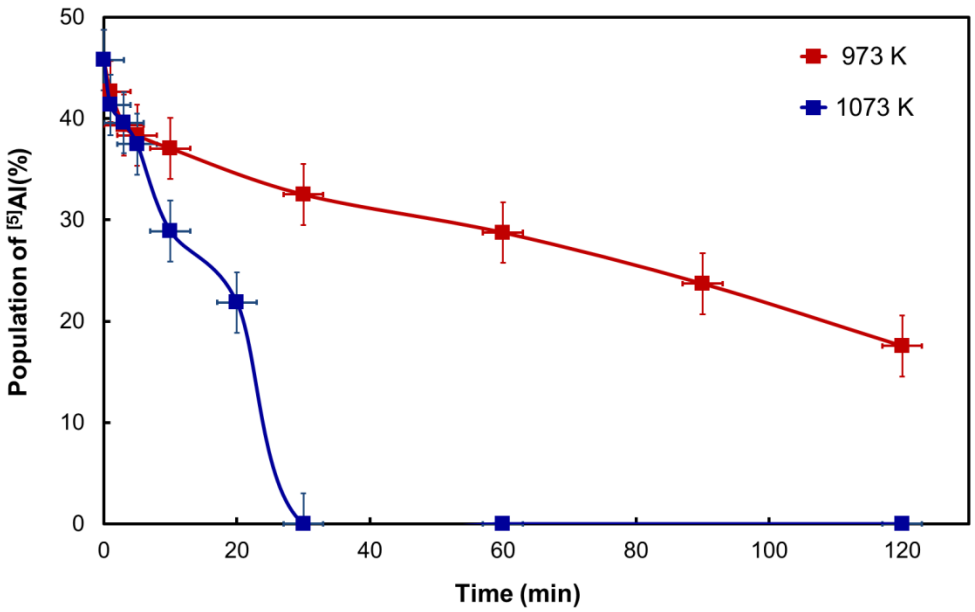

Figure 14 | Population of [5]Al in Al_2O_3 with annealing time.

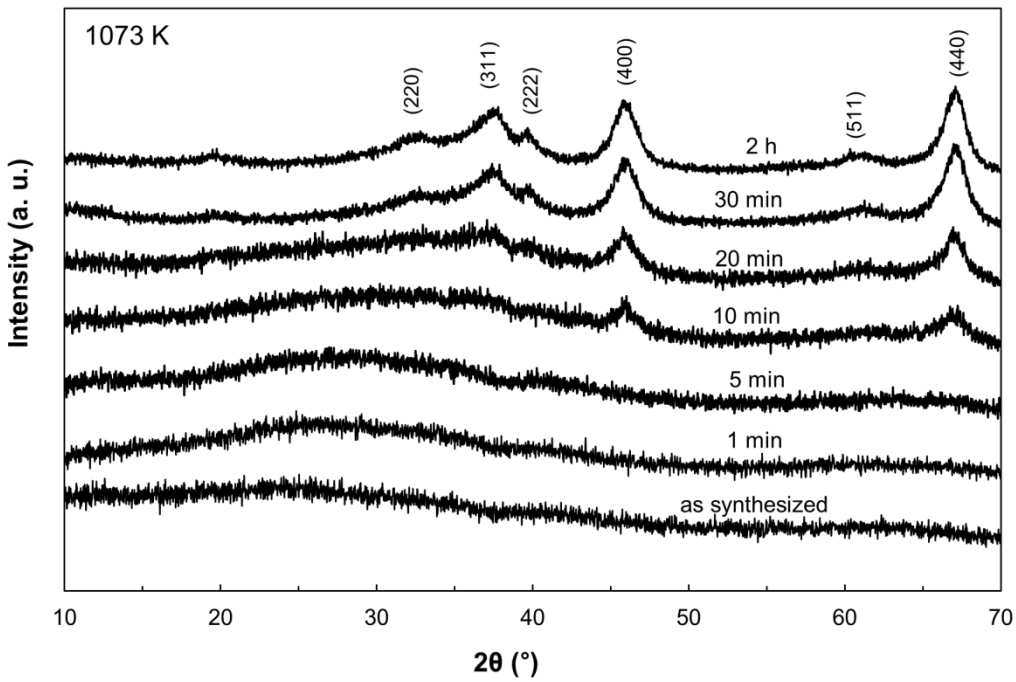

Figure 15| X-ray diffraction (XRD) patterns of amorphous Al_2O_3 and Al_2O_3 annealed for 1, 3, 5, 10, 20 and 120 min at 1073 K.

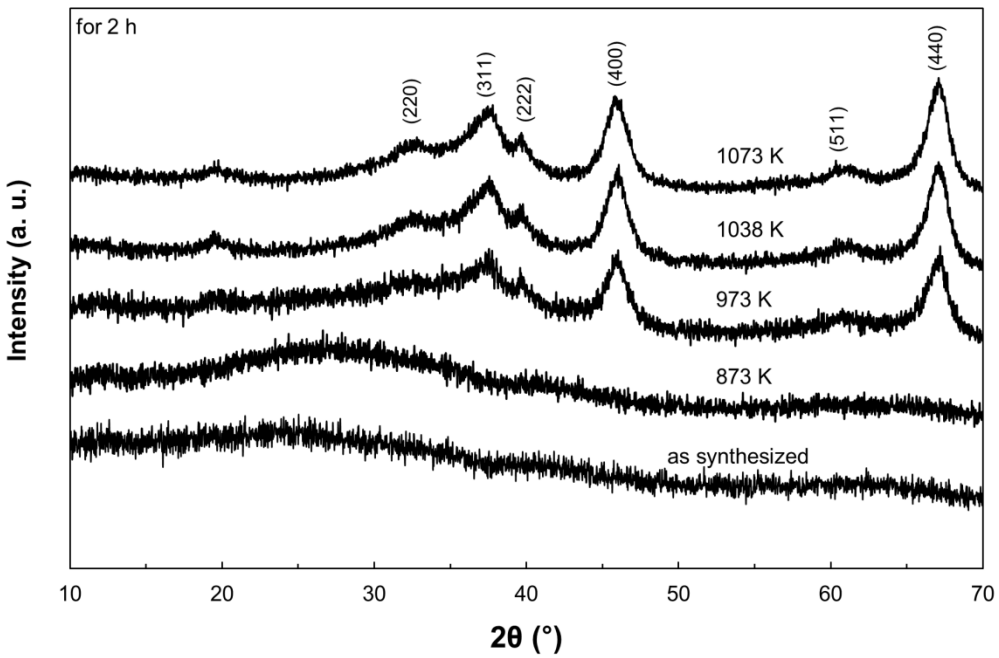

Figure 16| X-ray diffraction (XRD) patterns of Al_2O_3 annealed for 2 h at 873 K, 973 K, 1038 K and 1073 K.

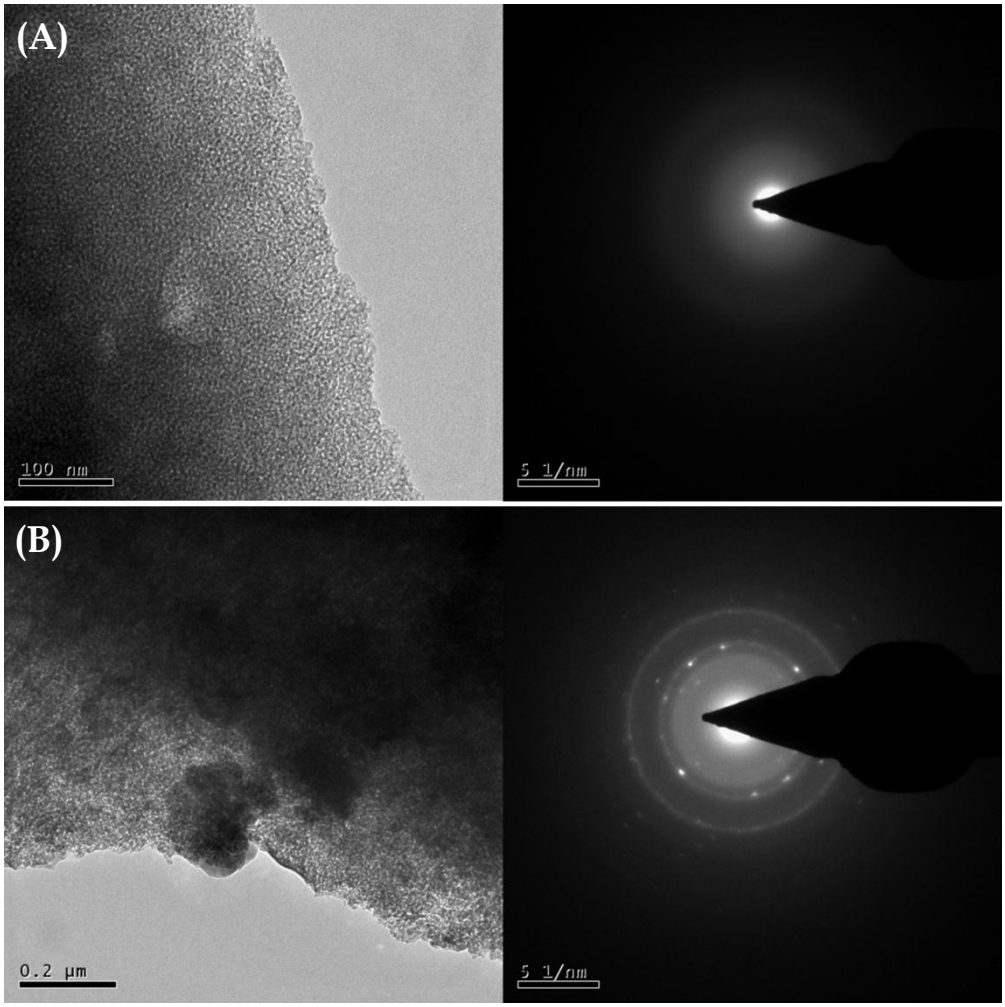

Figure 17| TEM images of amorphous and crystallized Al_2O_3.

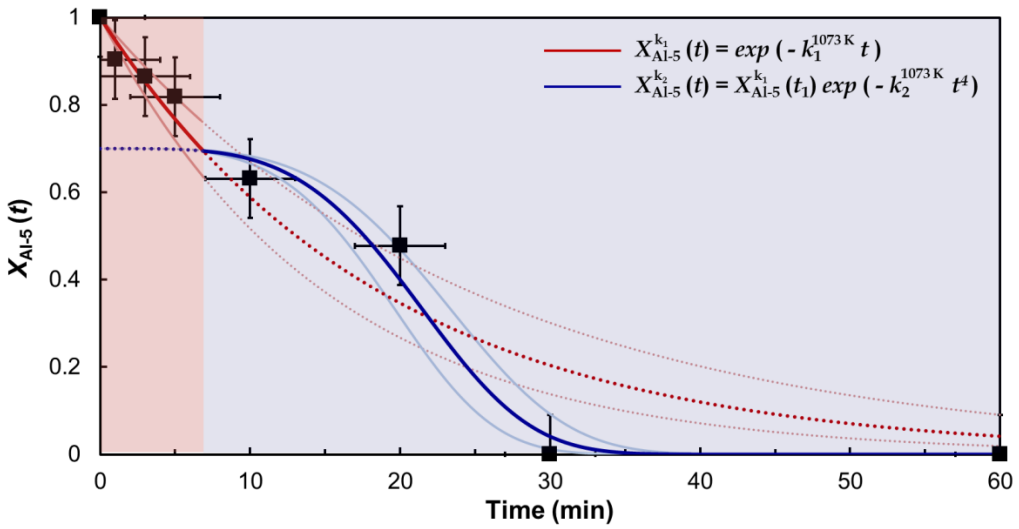

Figure 18 | Fractions of $^{[5]}Al$ in Al_2O_3 with annealing time at 1073 K. Red and blue lines refer to simulated mole fractions of $^{[5]}Al$ using an exponential function and Eq. 4, respectively (see text for details).

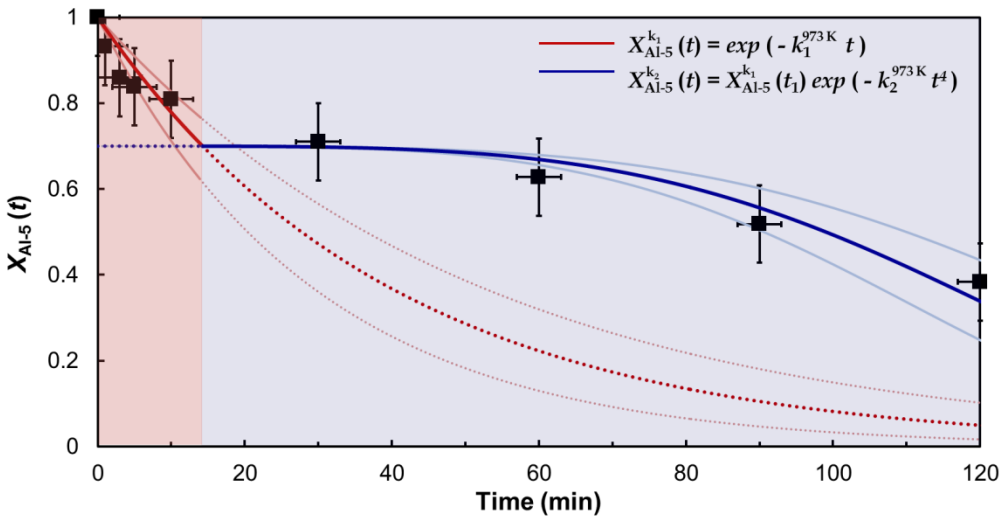

Figure 19| Fractions of [5]Al in Al_2O_3 with annealing time at 973 K. Red and blue lines refer to simulated mole fractions of [5]Al using an exponential function and Eq. 4, respectively (see text for details).

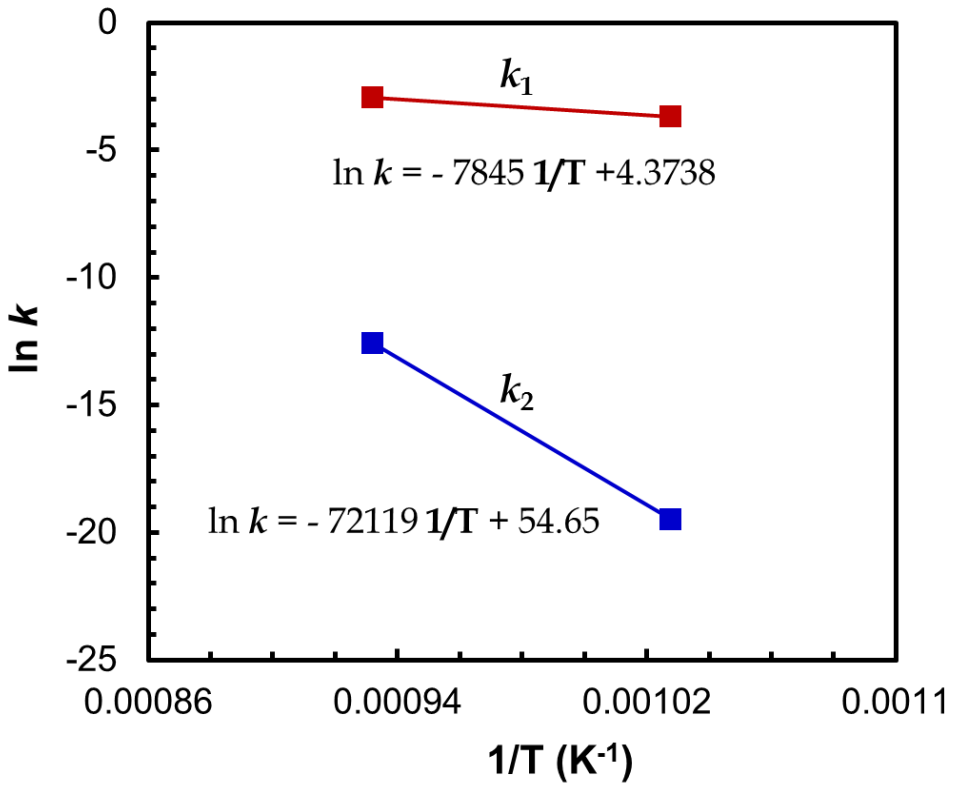

Figure 20| Arrhenius plot for Al_2O_3 annealed at 973 K and 1073 K.

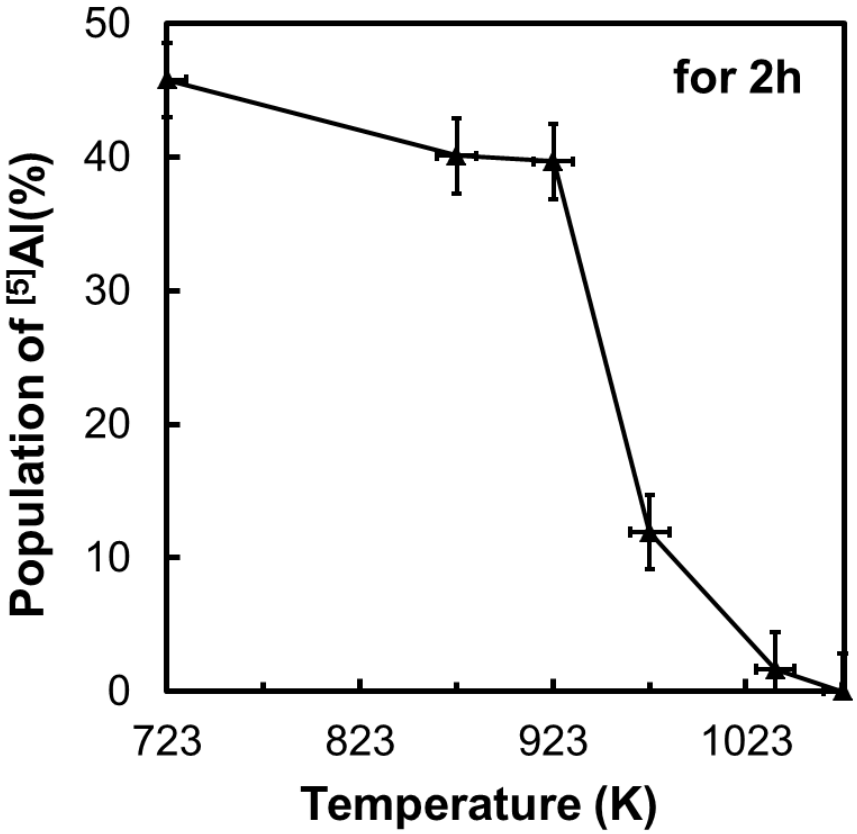

Figure 21 | Population of [5]Al in Al_2O_3 with annealing temperature.

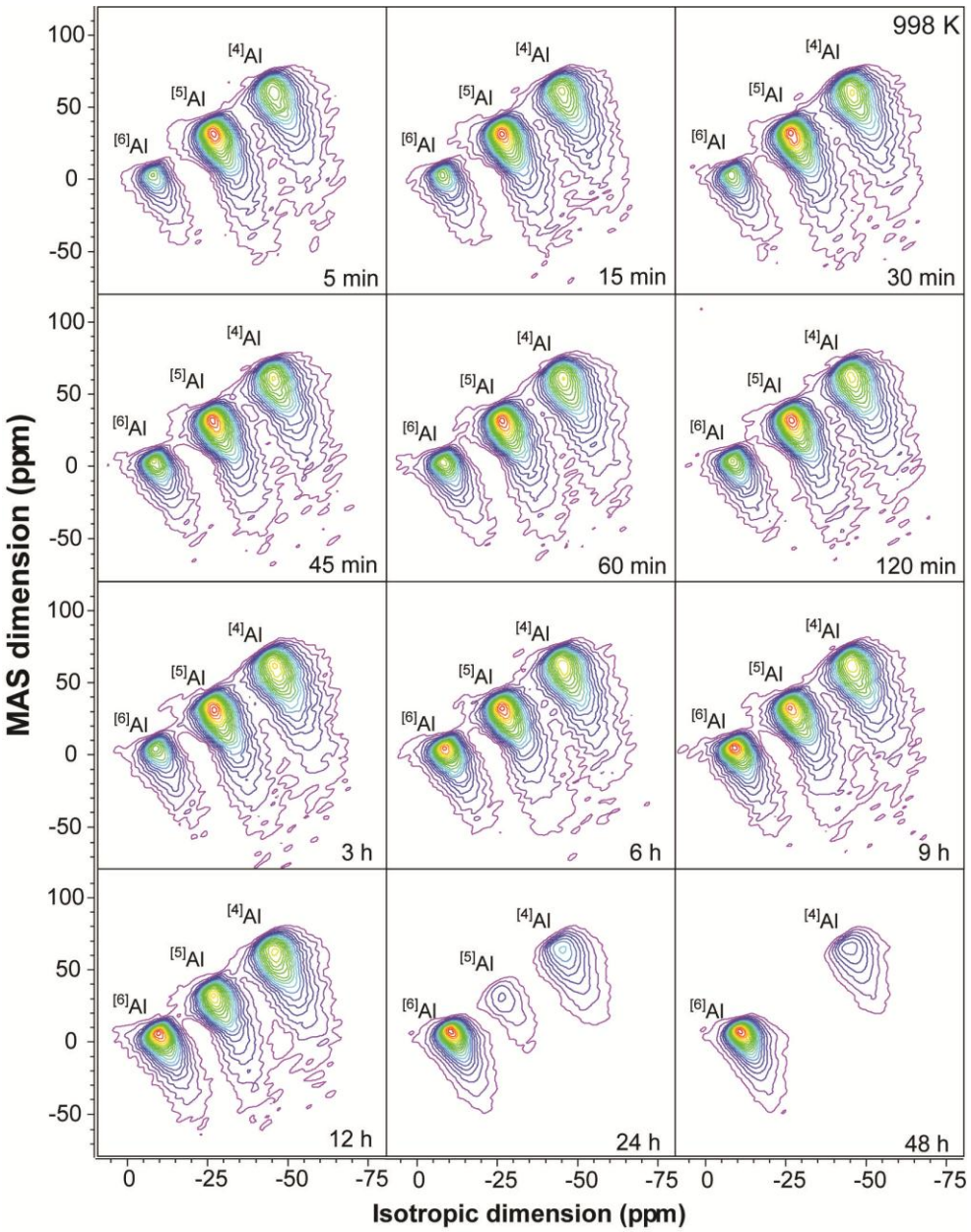

Figure 22| ^{27}Al 3QMAS NMR spectra for Al_2O_3 annealed at 998 K (the second attempt) with varying annealing time. Contour lines are drawn at 5% intervals from relative intensities of 8% to 98% with an added line at 4%.

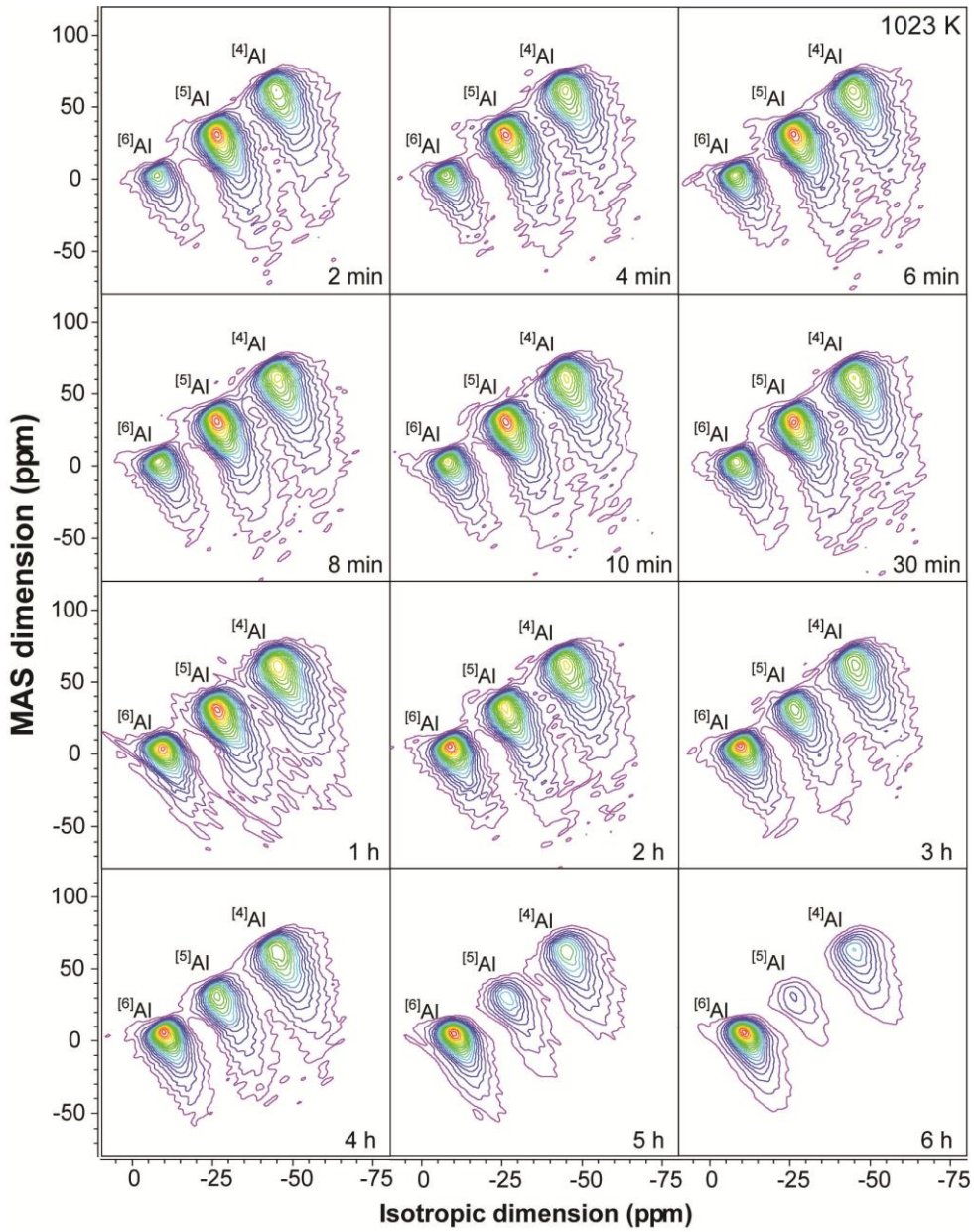

Figure 23 | ^{27}Al 3QMAS NMR spectra for Al_2O_3 annealed at 1023 K (the second attempt) with varying annealing time. Contour lines are drawn at 5% intervals from relative intensities of 8% to 98% with an added line at 4%.

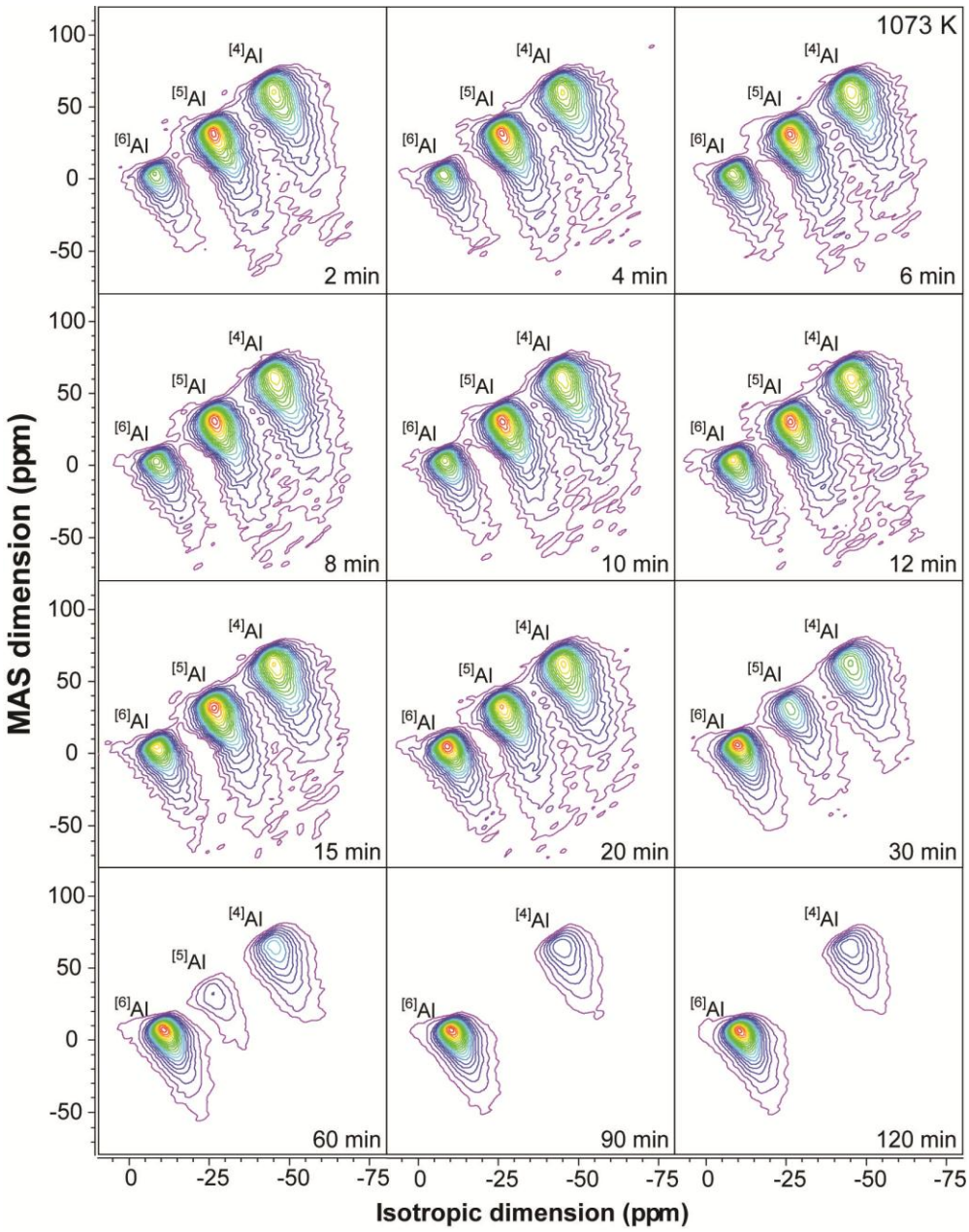

Figure 24 | ^{27}Al 3QMAS NMR spectra for Al_2O_3 annealed at 1073 K (the second attempt) with varying annealing time. Contour lines are drawn at 5% intervals from relative intensities of 8% to 98% with an added line at 4%.

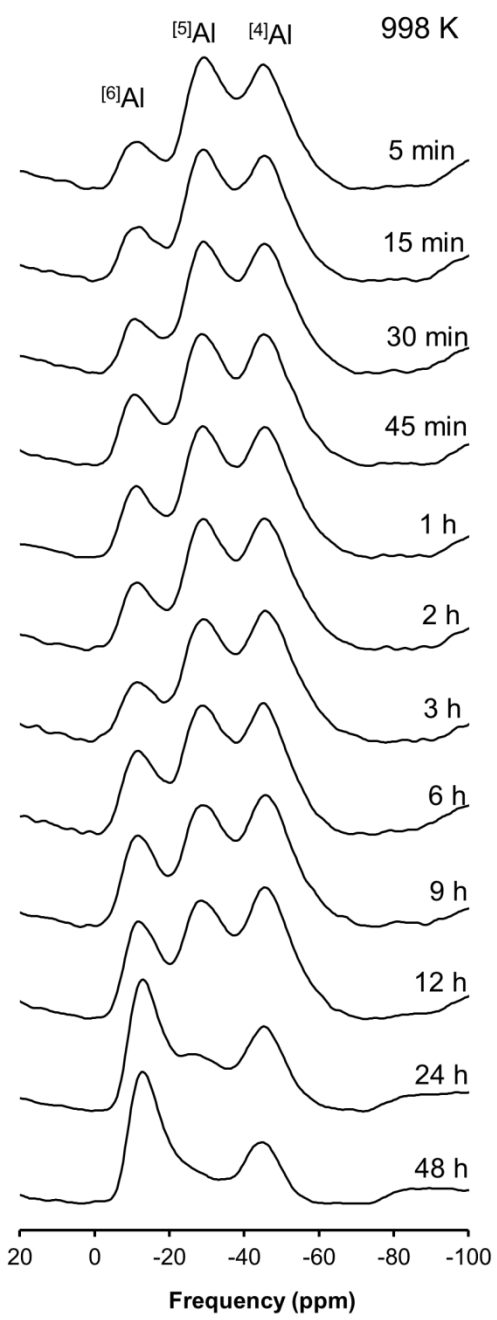

Figure 25| Total isotropic projections of ^{27}Al 3QMAS NMR spectra for Al_2O_3 annealed at 998 K (the second attempt) with varying annealing time.

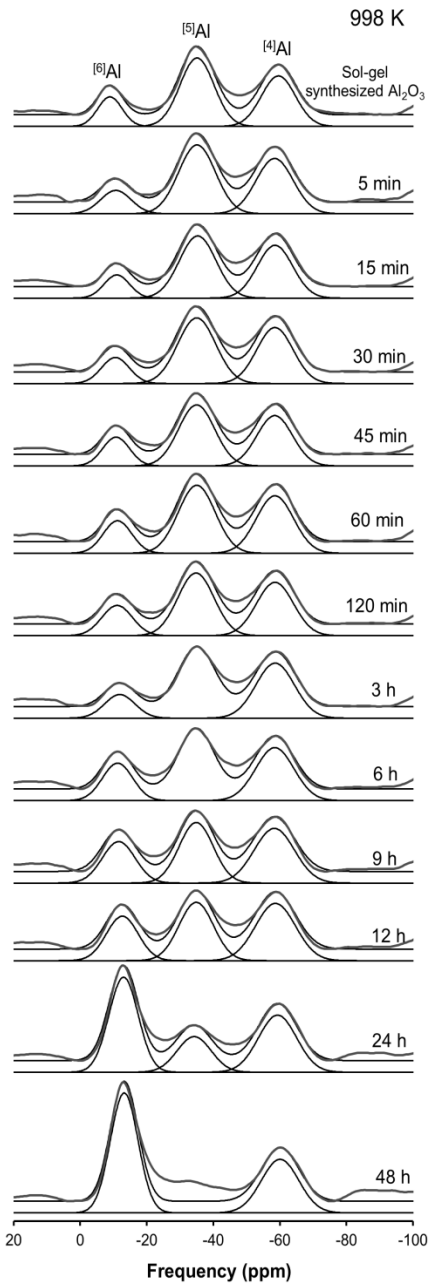

Figure 26| Results of simulating Gaussian functions (black lines) of isotropic projections of the ^{27}Al 3QMAS NMR spectra for Al_2O_3 annealed at 998 K (the second attempt) with varying annealing time. The gray lines refer to the experimental spectra rotated 30^0 clockwise.

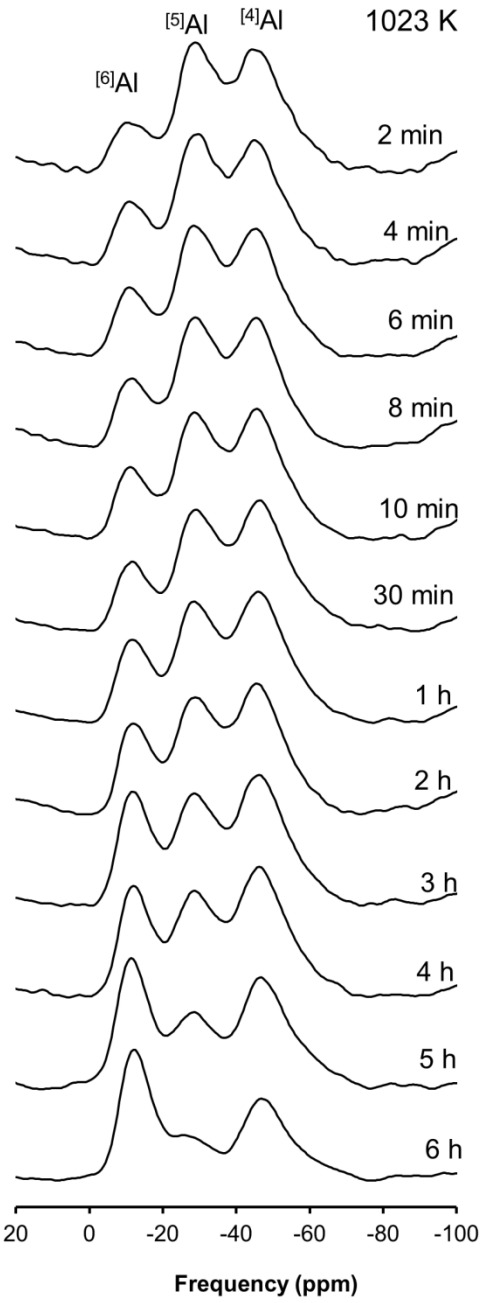

Figure 27| Total isotropic projections of ^{27}Al 3QMAS NMR spectra for Al_2O_3 annealed at 1023 K (the second attempt) with varying annealing time.

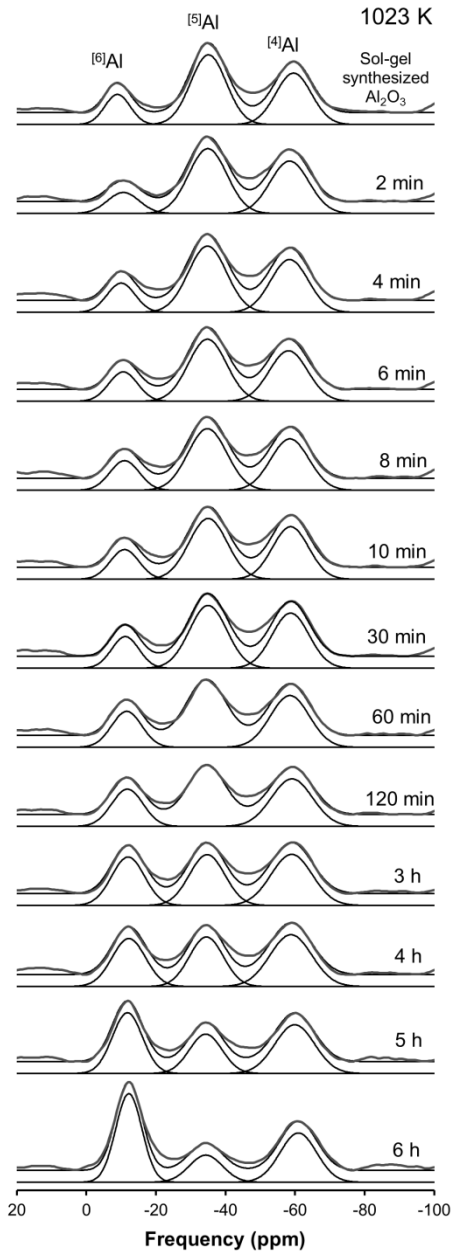

Figure 28| Results of simulating Gaussian functions (black lines) of isotropic projections of the ^{27}Al 3QMAS NMR spectra for Al_2O_3 annealed at 1023 K (the second attempt) with varying annealing time. The gray lines refer to the experimental spectra rotated 30^0 clockwise.

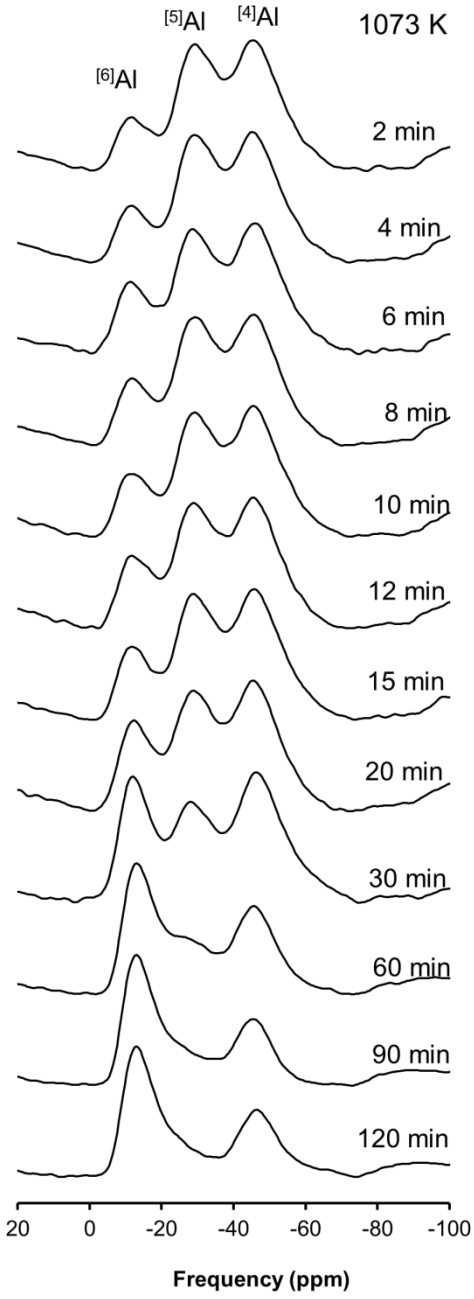

Figure 29| Total isotropic projections of ^{27}Al 3QMAS NMR spectra for Al_2O_3 annealed at 1073 K (the second attempt) with varying annealing time.

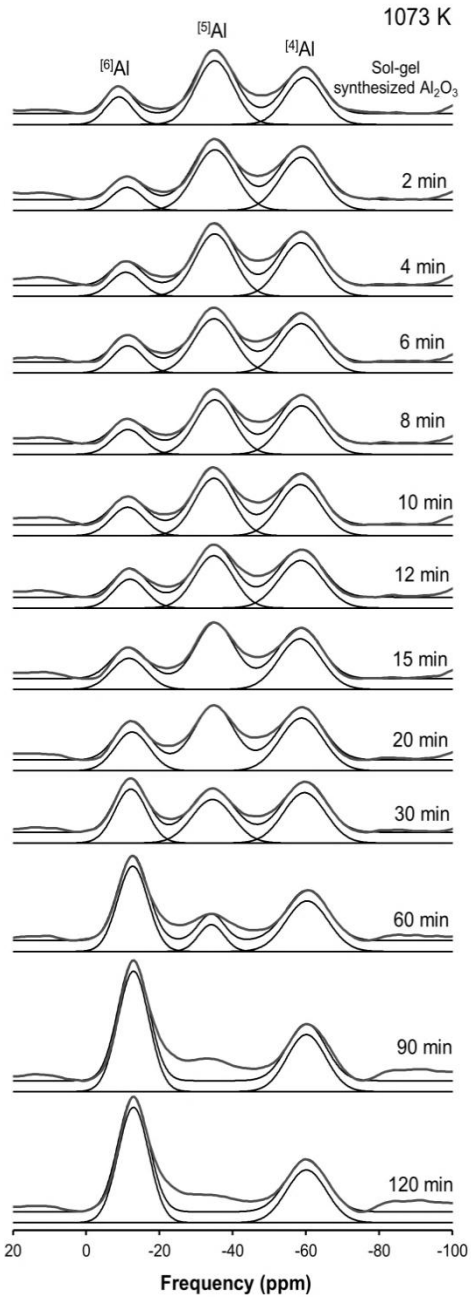

Figure 30| Results of simulating Gaussian functions (black lines) of isotropic projections of the ^{27}Al 3QMAS NMR spectra for Al_2O_3 annealed at 1073 K (the second attempt) with varying annealing time. The gray lines refer to the experimental spectra rotated 30^0 clockwise.

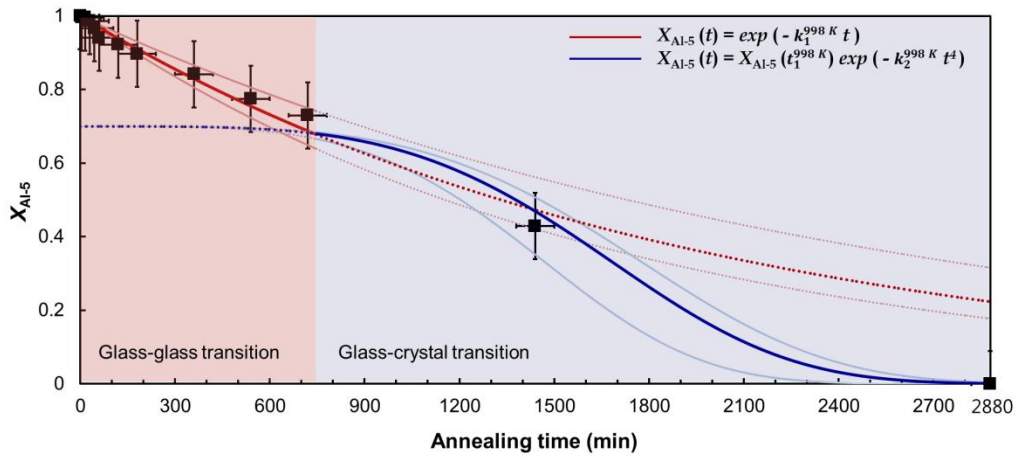

Figure 31 | Fractions of $^{[5]}Al$ in Al_2O_3 with annealing time at 998 K (the second attempt). The relationship is simulated by using exponential functions (red and blue lines).

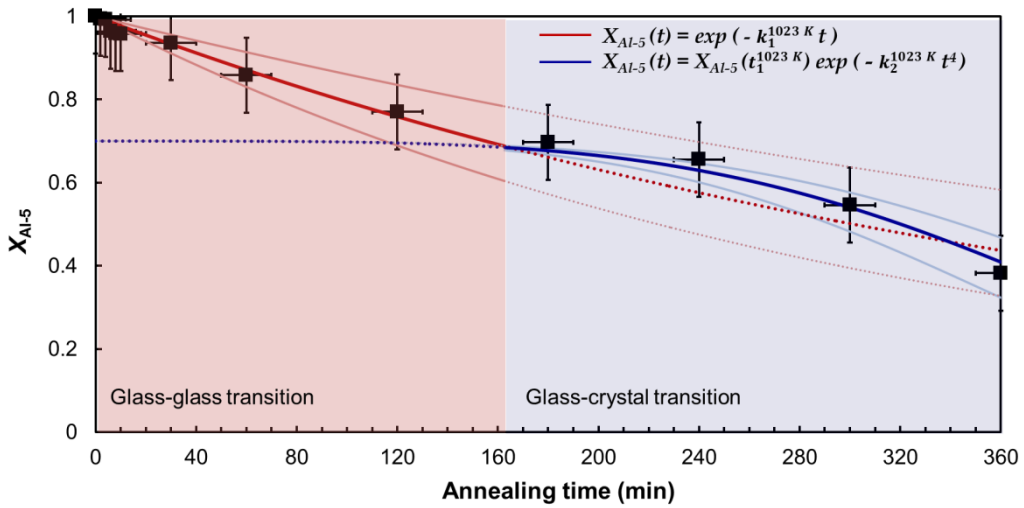

Figure 32| Fractions of [5]Al in Al_2O_3 with annealing time at 1023 K (the second attempt). The relationship is simulated by using exponential functions (red and blue lines).

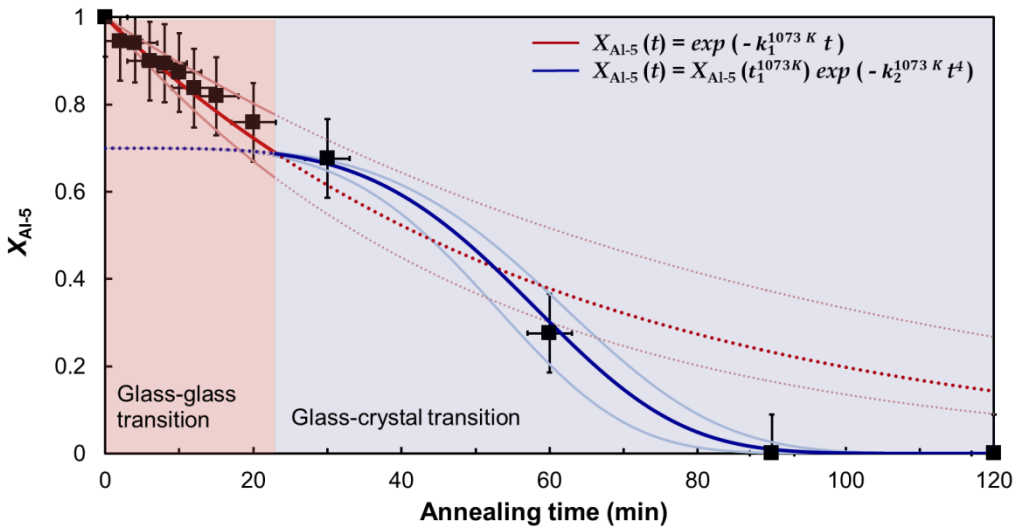

Figure 33| Fractions of [5]Al in Al_2O_3 with annealing time at 1073 K (the second attempt). The relationship is simulated by using exponential functions (red and blue lines).

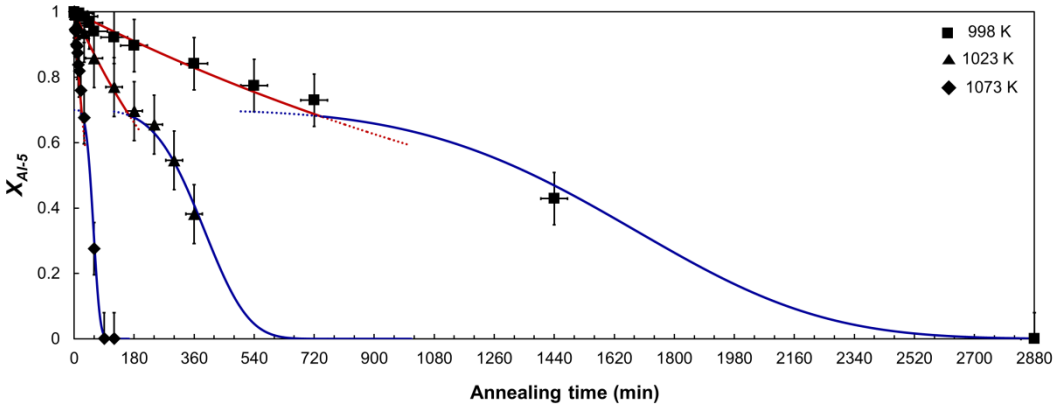

Figure 34| Population changes of $^{[5]}Al$ in Al_2O_3 annealed at 998K, 1023 K and 1073 K (the second attempt).

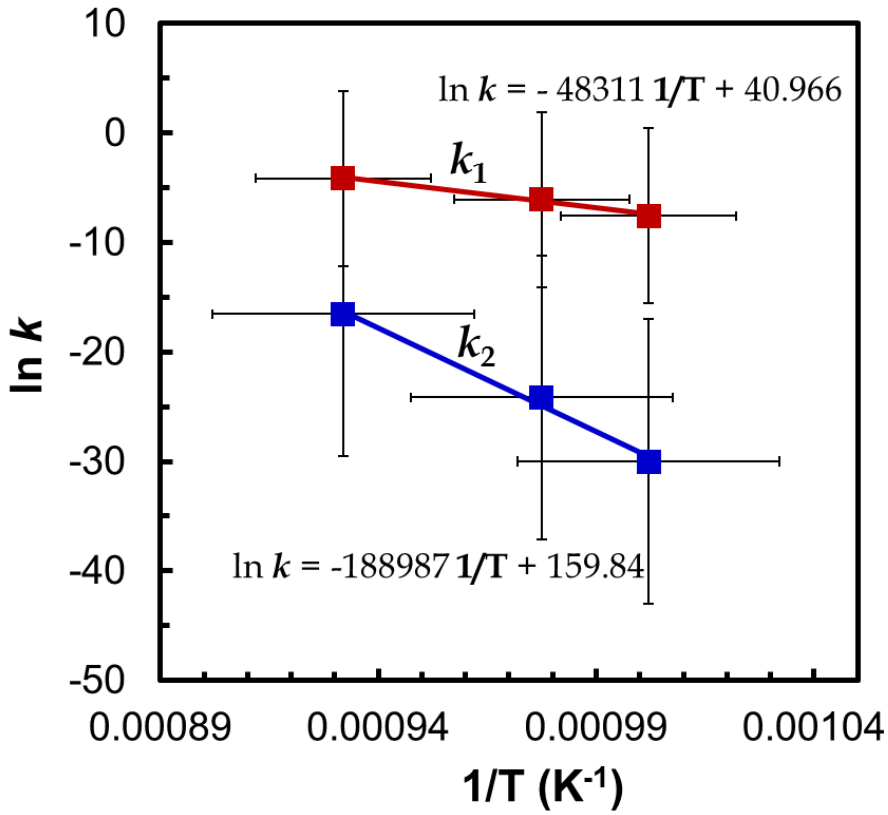

Figure 35| Arrhenius plot for Al_2O_3 annealed at 998 K, 1023 K and 1073 K (the second attempt).

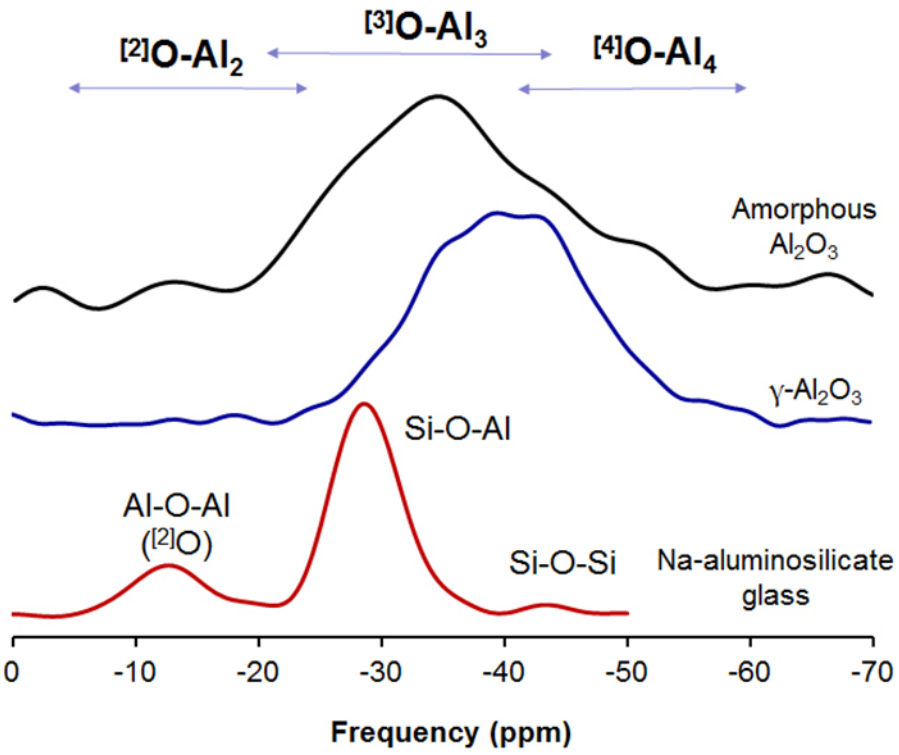

Figure 36| ^{17}O MAS NMR spectra for sol-gel synthesized Al_2O_3 (black) and γ-Al_2O_3 (blue) and Na-aluminosilicate glass (red).

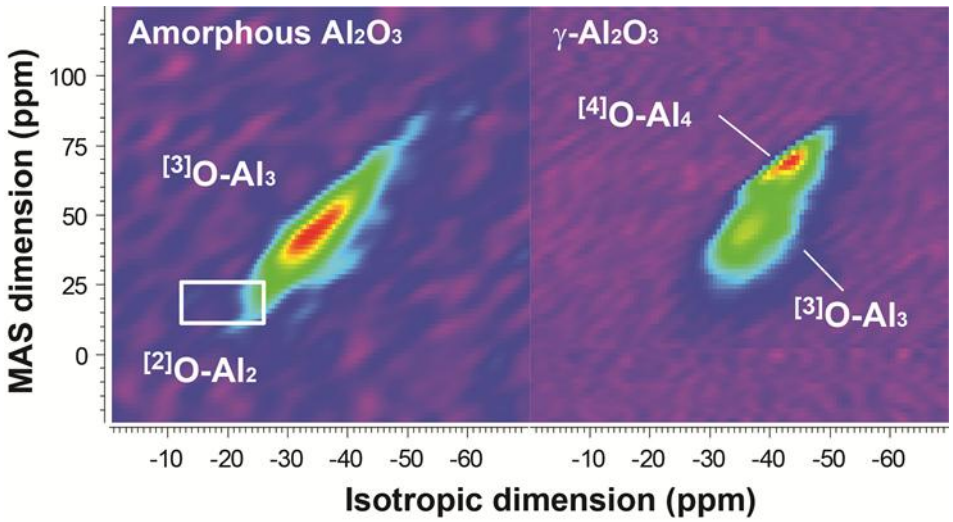

Figure 37| ^{17}O 3QMAS NMR spectra for sol-gel synthesized Al_2O_3 (left) and γ-Al_2O_3 (right).

(A)

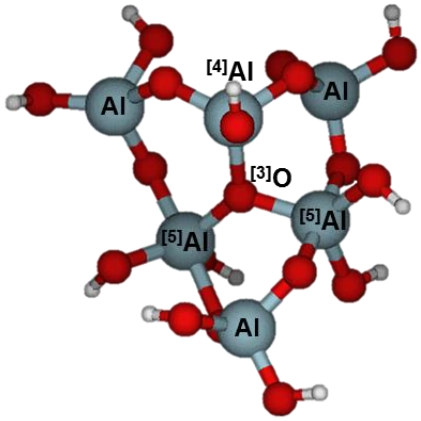

(B)

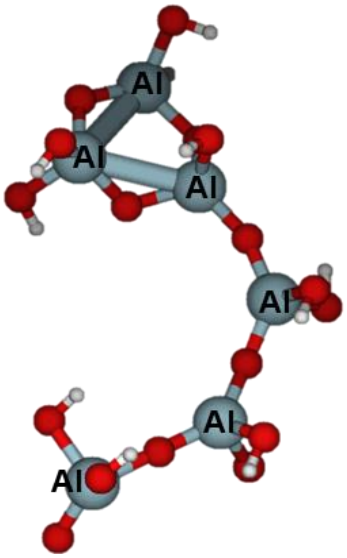

Figure 38 | Atomistic model for amorphous Al_2O_3 cluster including $^{[3]}O$. Gray, red, white atoms are Al, O, H, respectively. (A) Starting model for amorphous Al_2O_3 cluster with 2 of $^{[5]}Al$ and 1 of $^{[4]}Al$ for the central network. (B) Result of optimization by Gaussian 03.

(A)

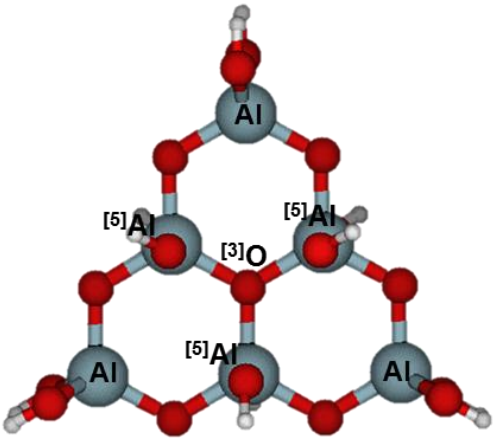

(B)

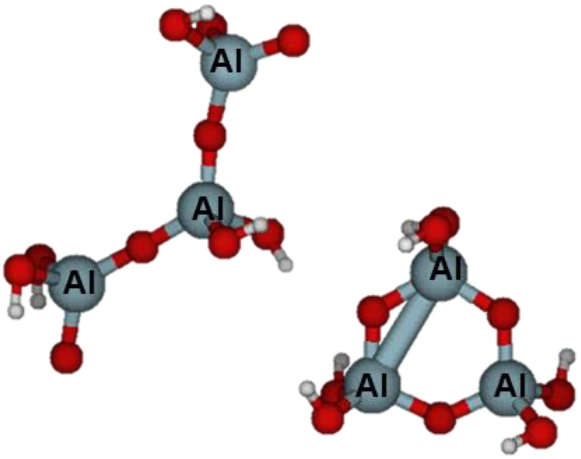

Figure 39| Atomistic model for $^{[3]}O$ in amorphous Al_2O_3 cluster including $^{[3]}O$. Gray, red, white atoms are Al, O, H, respectively. (A) Starting model for amorphous Al_2O_3 cluster with 3 of $^{[5]}Al$ for the central network. (B) Result of optimization by Gaussian 03.

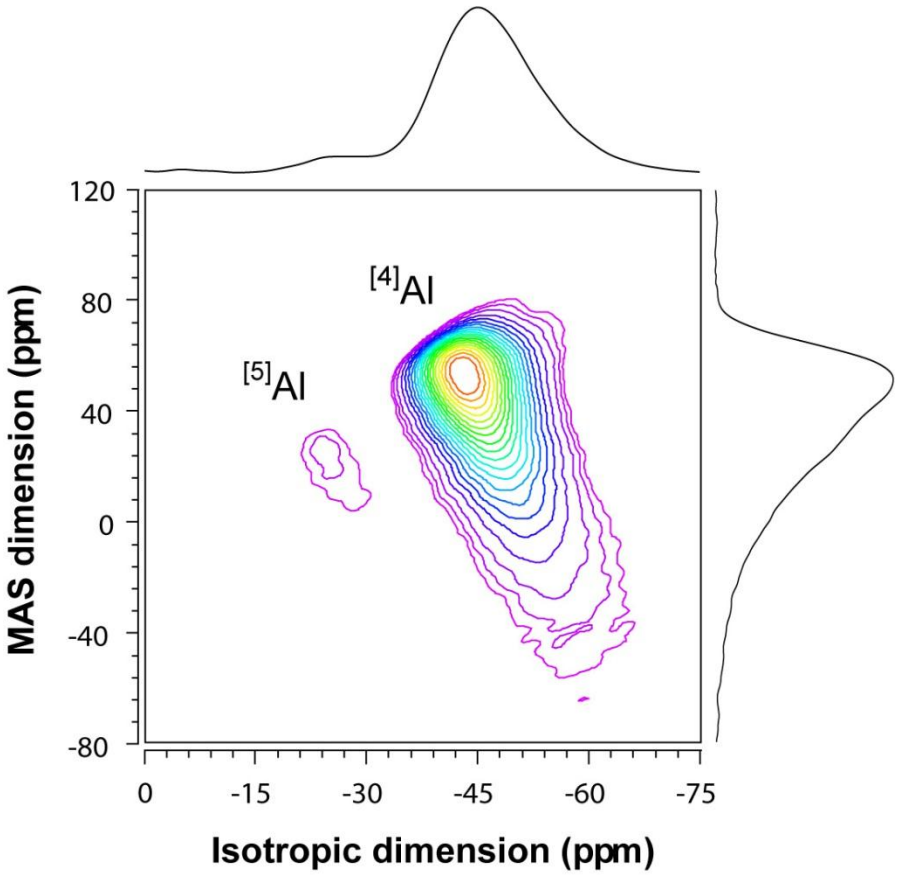

Figure A1 | ^{27}Al 3QMAS NMR spectra of pyrope ($Mg_3Al_2Si_3O_{12}$) glass. Contour lines are drawn at 5% intervals from relative intensities of 3% to 93%, with an added line at 5%.

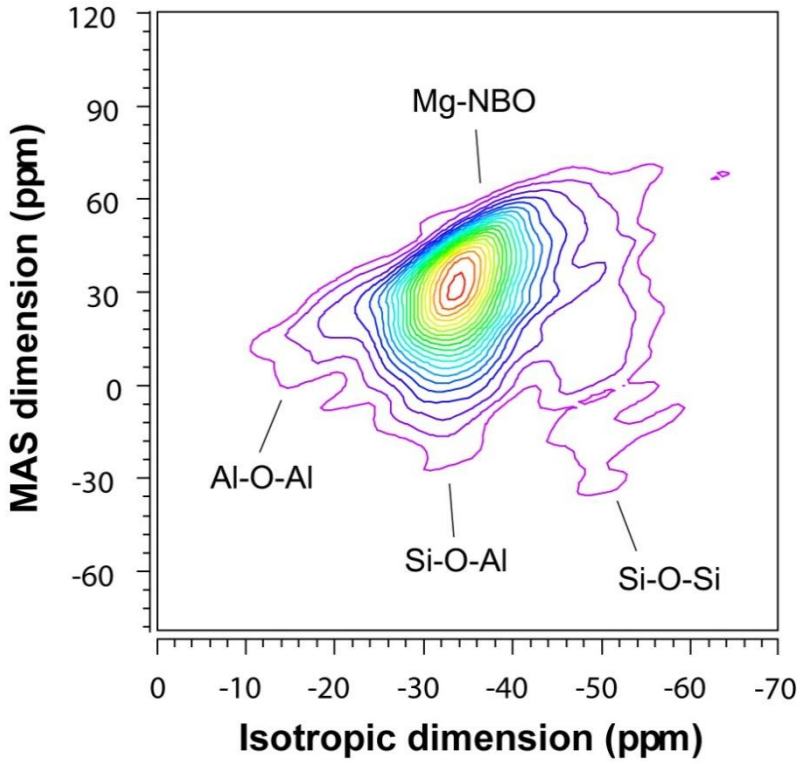

Figure A2| ^{17}O 3QMAS NMR spectra for pyrope ($Mg_3Al_2Si_3O_{12}$) glass. Contour lines are drawn at 5% intervals from relative intensities of 3% to 93%, with an added line at 4%.

Appendix section

Appendix I. Atomic Environments of Pyrope Glass

One of important Mg-aluminosilicate glasses, pyrope ($Mg_3Al_2Si_3O_{12}$), structure has been revealed by ^{27}Al and ^{17}O 3QMAS NMR. To prepare the sample, the weighed powders (3 mol of MgO, 1 mol Al_2O_3, 3 mol of ^{17}O enriched SiO_2) were mixed by grinding in an agate mortar. Approximately 0.2 wt% of cobalt oxide was mixed together in order to enhance spin–lattice relaxation. The sample was then heated in a Pt crucible to 1893 K for about 6 h and melted at 1913 K above its melting temperature for 1 h, and quenched into glasses by plunging the bottom of the Pt crucible into a water bath. NMR experiments were conducted using a Varian 400 solid-state NMR spectrometer (9.4 T) with a 3.2 mm zirconia rotor in a Varian double-resonance probe. ^{27}Al 3QMAS NMR spectra were collected at Larmor frequency 104.23 MHz with 18 kHz sample spinning speed. ^{17}O 3QMAS NMR spectra were at 54.23 MHz with 15 kHz spinning speed. In both 3QMAS NMR experiments, FAM-based shifted echo pulse sequences were used with a relaxation delay of 1 s. Figure A1 shows ^{27}Al 3QMAS NMR spectra of pyrope ($Mg_3Al_2Si_3O_{12}$) glass, and it exhibits well resolved Al coordination environments, characterized with mostly $^{[4]}Al$ and a minor fraction of $^{[5]}Al$. Figure A2 presents ^{17}O 3QMAS NMR spectra for pyrope ($Mg_3Al_2Si_3O_{12}$) glass, showing Al-O-Al, Si-O-Al, Si-O-Si and Mg-NBO peaks.

Appendix II. C. V.

Saebom Ryu

ryusaebo@snu.ac.kr

EDUCATION

2009. 8 B. S. Seoul National University, School of Earth and Environmental Sciences

RESEARCH EXPERIENCE

2009 ~ 2012 Research assistant, Seoul National University

2012 Teaching assistant, Seoul National University

HONORS & AWARDS

2011. 5 최우수포스터상, 2011 추계지질과학연합 학술발표회

2011. 9 성적우수 장학금, 서울대학교

2011. 3 강의·연구지원 장학금, 서울대학교

2009. 9 전재규 장학금, 전재규장학재단

PUBLICATIONS

Ryu, S. and Lee, S. K. (2012) A Solid-State NMR Study of Coordination Transformation in Amorphous Aluminum Oxide: Implication for

Crystallization of Magma Ocean. Journal of Mineralogical Society of Korea, 25(4), 283-293

CONFERENCES

2012. 5 비정질 알루미나 결정화 과정의 반응속도론 연구를 통한 마그마바다의 결정화 과정 이해 (구두발표), 2012 한국암석학회 및 (사)한국광물학회 공동학술발표회

2011. 10 Structural Transitions in Alumina and Aluminate Melts: Implication for Crystallization of Magma Ocean (Poster), 2011 Fall Meeting of Geological Society of Korea

2011. 10 Structure of Alumina Glass: A View from Al-27 NMR (Poster), 9th Silicate Melt Workshop, France

국문초록

지구가 마그마 바다 상태에서 현재의 층상화된 내부 구조로 분화되는 진화과정의 체계적인 이해를 위하여 규산염 용융체와 같은 비정질 산화물의 결정화 과정 메커니즘 규명이 필요하다. 이를 위하여 결정화 과정에서 수반하는 용융체의 원자구조 변화를 실험적으로 측정하여 결정화 과정을 정량적으로 정립할 수 있다. 본 연구에서는 고상 핵자기 공명 분광분석(NMR)을 이용하여 졸겔법으로 합성한 비정질 알루미나(Al_2O_3)의 온도-가열시간 변화에 따른 원자구조 변화로부터, 비정질-결정질 상전이 과정을 원자단위에서 규명하였다. 비정질 Al_2O_3 의 ^{27}Al 3QMAS NMR 실험 결과 다량의 배위수 4, 5 의 알루미늄($^{[4,5]}$Al)과 소량의 배위수 6 인 알루미늄($^{[6]}$Al)이 명확히 구분되어 관찰되었고, 973 K 와 1073 K 에서 각각 가열시간을 증가시킬수록 배위수 5 인 알루미늄($^{[5]}$Al)이 감소하였다. 본 연구에서는 $^{[5]}$Al 의 분율을 결정화의 지표로 이용하여 ^{27}Al 3QMAS NMR 결과를 정량분석하였다. 가열시간(t)의 증가에 따른 $^{[5]}$Al 의 분율 감소는 $\exp(-k_1 t)$ 형태의 함수를 따르는 반응의 전반부와 $\exp(-k_2 t^4)$의 형태로 표현되는 후반부의 두 구간으로 나뉘어졌다. XRD 와 TEM 분석을 통해 과정의 초기구간에서는 결정질 알루미나의 특징이 관찰되지 않는 것을 확인하였고, 후반부에서 결정질이 관찰되는 것을 확인하였다. 또한 각 구간에서의 활성화 에너지를 계산한 결과, 반응 후반부의 활성화 에너지가 전반부보다 더 큰 것으로 나타났으며, 이는 비정질 내에서의 구조전이가 결정화보다 동역학적으로 발생하기 쉬운 반응임을 지시한다. 시료 내 잔류하는 유기물 혹은 표면의 수산기에 의한 영향으로 계산된 활성화 에너지 값에는 오차가 있을 수 있다.

본 연구를 통해 점진적인 원자구조의 변화로 관찰되는 단성분계 비정질 산화물의 결정화 과정이 비정질 내 구조적 무질서도 변화와 결정화의 구분되는 두 단계로 구성됨을 최초로 밝혔다. 결정화 과정에서 서로 다른 속도로 설명되는 두 과정이 존재한다는 것은 마그마 바다의 결정화를 비롯한 지구물질의 결정화 과정에서 원자 구조의 변화에 의한 물질의 거시적인 성질 변화가 결정화가 시작되기 전에도 발생할 수 있음을 시사하며, 마그마 바다의 지속기간을 예측하는 새로운 관점을 제시한다. 결정이 형성 되기 전 용융체 내에서의 구조전이에 소요되는 시간이 마그마 바다의 지속기간 계산에 포함되어야 하며, 기존의 열분석법으로 얻어지는 하나의 결정화 반응속도론 상수만으로는 정확한 예측에 어려움이 있음을 지시한다. 또한 마그마 바다의 대류모델을 연구할 때, 단순히 결정의 분율만을 고려하여 점성도의 변화를 적용할 것이 아니라 비정질 내에서의 구조전이에 의한 점성도의 변화도 고려해야 함을 의미한다. 이와 같은 해석은 마그마 바다를 이해하기 위해 모델시스템을 비정질 알루미나로 설정하고 결정화 과정을 원자 단위에서 관찰하여 이룬 첫 실험적 성과이다. 이러한 연구 결과는 다양한 자연계의 다성분계 규산염 용융체 결정화 과정 및 마그마 바다의 분화와 지구의 화학적 진화에 대한 원자 단위의 이해증진에 도움을 줄 것이다.

주요어: 비정질 Al_2O_3, 고상 핵자기 공명 분광분석, 결정화 반응속도론, 마그마 바다

학번: 2009-22950